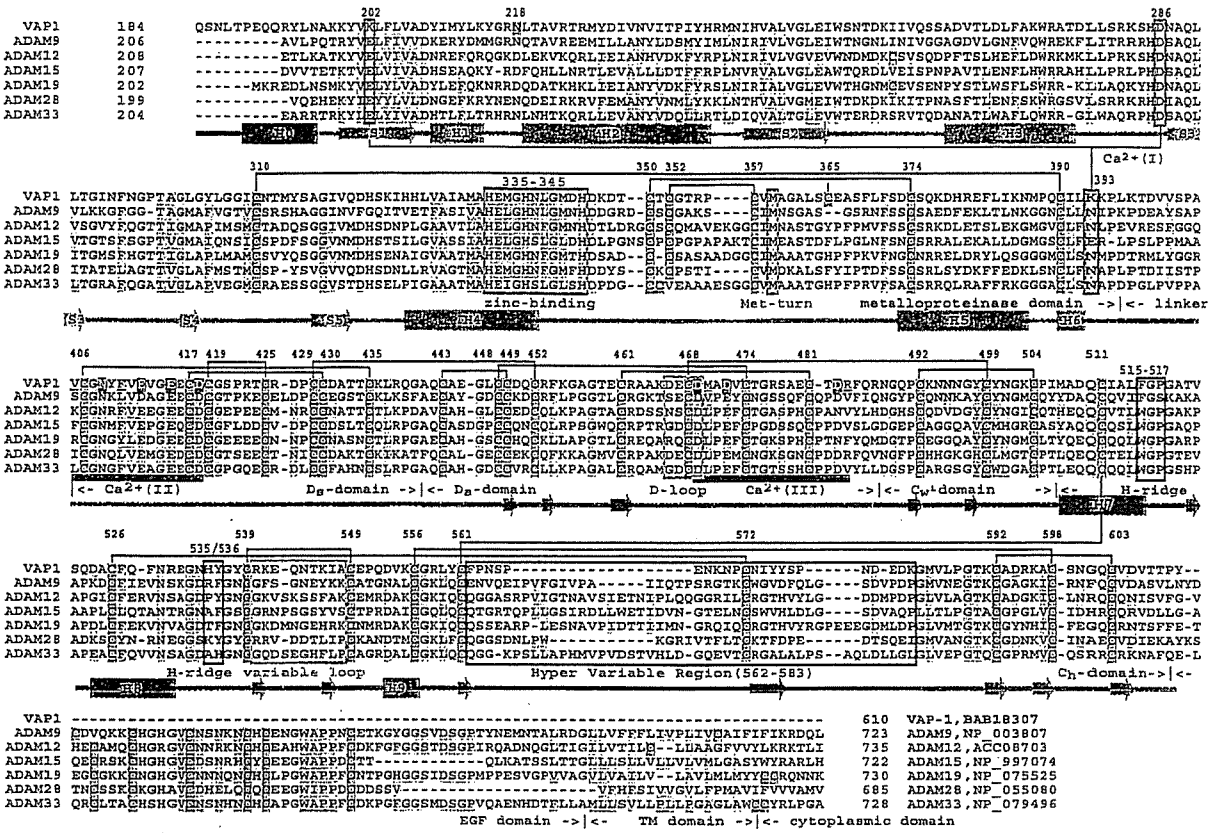

Figure 2 Sequence alignments of VAP1 and human ADAMs. The cysteinyl residues and the conserved residues are shaded in pink and yellow, respectively. Disulfide bridges, secondary structures and domains are drawn schematically. The HVR, calcium-binding site I, catalytic site and disintegrin-loop (D-loop) are boxed in blue, red, green and cyan, respectively. The hydrophobic ridges (H-ridges) are indicated. Calcium-binding sites II and III and the coordinating residues (shaded in red) are indicated. The NCBI accession numbers for the sequences are indicated.

M-domain structure suggests that most ADAMs have a Ca^{2+}-binding site (designated Ca^{2+}-binding site I) opposing the active-site cleft; however, in VAP1, the distal ammonium group of Lys202 substitutes for the Ca^{2+} ion (Figure 1D). Replacement of the calcium-coordinating glutamate residue with lysine also occurs in ADAM16, ADAM25 and ADAMs38–40 (Supplementary Figure 1).

C-shaped arm

The D-domain follows the M-domain, with a short linker that allows slightly variable domain orientations at V405 as a pivotal point (Figure 3C). The D-domain is further divided into two structural subdomains (Figure 3), the 'shoulder' (D_s-domain, residues 396–440) and the 'arm' (D_a-domain, residues 441–487). The D_s- and D_a-domains constitute a continuous C-shaped arm, together with the following N-terminus region of the C-domain which we designate the 'wrist' (C_w-domain, residues 488–505). There are three disulfide bonds in the D_s-domain, three in the D_a-domain and one in the C_w-domain. The subdomains are connected by single disulfide bridges (Figures 2 and 3A) with slightly variable angles (Figure 3B).

Both the D_s- and D_a-domains contain structural calcium-binding sites. In the D_s-domain, the side-chain oxygen atoms in residues Asn408, Glu412, Glu415 and Asp418, and the carbonyl oxygen atoms of Val405 and Phe410 are involved in pentagonal bipyramidal coordination and constitute Ca^{2+}-binding site II (Figures 2 and 3A). Notably, these residues are strictly conserved among all known ADAMs (Supplementary Figure 1). However, the side-chain oxygens of Asp469, Asp472 and Asp483, and carbonyl oxygens of Met470 and Arg484 form the corners of a pentagonal bipyramid to the calcium ligand and constitute the D_a-domain Ca^{2+}-binding site III (Figures 2 and 3A) and these residues are highly conserved among ADAMs except ADAM10 and ADAM17 (Supplementary Figure 1). Because of the few secondary-structural elements, bound calcium ions and the disulfide bridges are essential for the structural rigidity of ADAM's C-shaped arm. The RGD-containing disintegrin trimestatin (Fujii *et al*, 2003) has a similar structure with the D_a-domain (r.m.s.d of 1.24 Å, Figure 3B); however, no disintegrins have been shown to bind Ca^{2+} ions.

Using isolated D-domains or portions thereof, numerous ADAMs and P-III SVMPs have been shown to interact specifically with particular integrins (Evans, 2001; White, 2003; Calvete *et al*, 2005). However, the disintegrin-loop is packed against the C_w-domain and a disulfide bridge (Cys468–Cys499) further stabilizes the continuous structure (Figure 3A). Therefore, the disintegrin-loop is inaccessible for protein binding.

Hand domain

The 'hand' domain (C_h-domain, residues 505–610) follows the C_w-domain. The C_h-domain, together with the C_w-domain, constitutes a novel fold (Figure 4A). In either crystal form, VAP1 dimers interact with molecules of neighboring

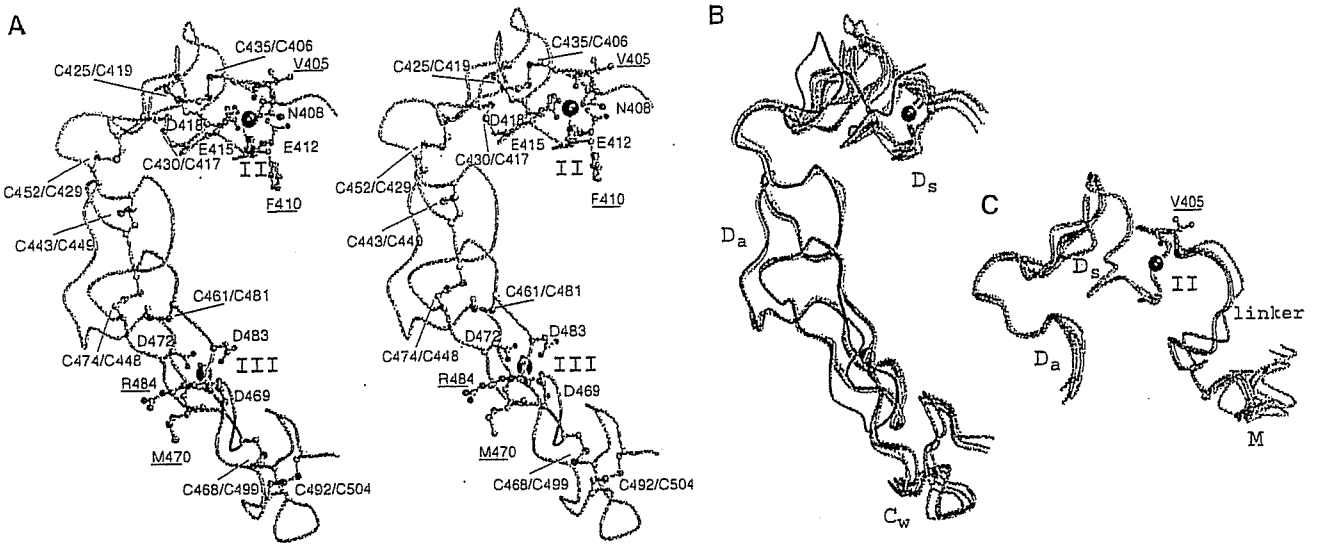

Figure 3 Arm structure. (A) Arm structure *in stereo*. The D_s-, D_a-, and C_w-domains are in cyan, pink and light green, respectively. The calcium-coordinating residues and the disulfide bridges are shown in red and green, respectively. The residues with carbonyl oxygen atoms involved in calcium coordination are underlined. Calcium ions are represented as black spheres. The disintegrin-loop (DECD) is in blue. (B) Superimposition of the four D_a-domains of VAP1 and trimestatin (1J2L). Trimestatin and its RGD loop are shown in red and blue, respectively. (C) Superimposition of the four D_s-domains. The linker between the M- and D_s-domains is shown in gray. Val405 at the pivotal point is indicated.

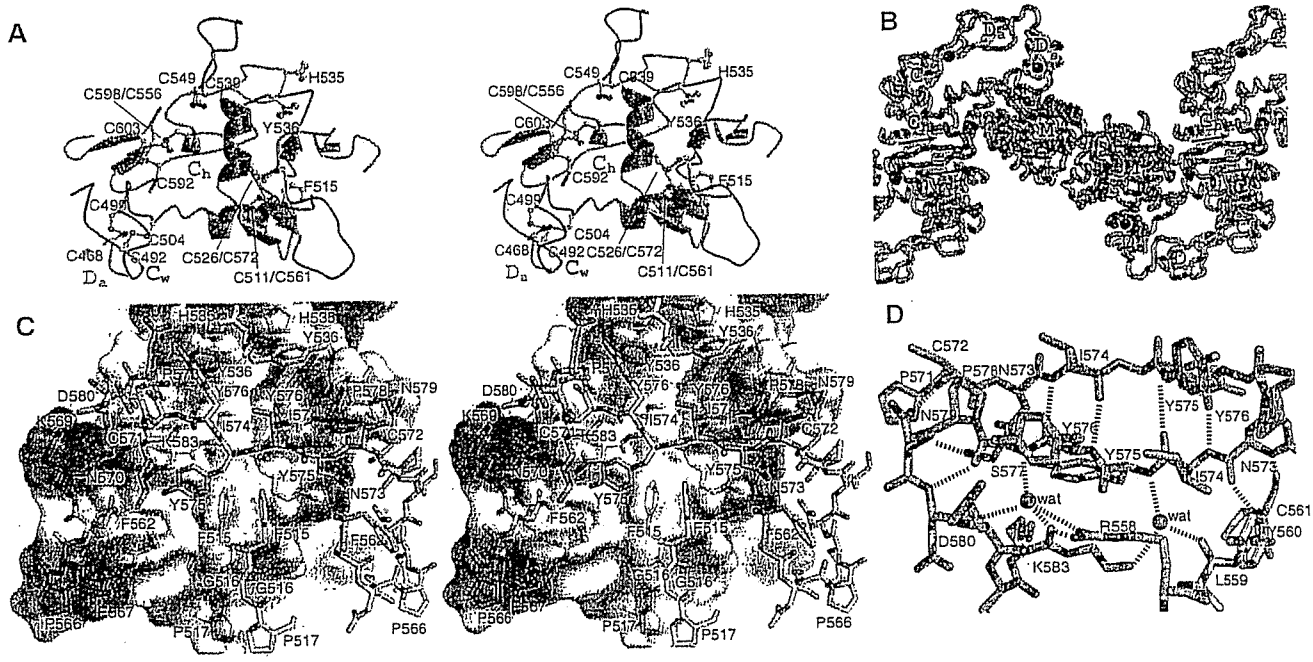

Figure 4 C-domain architecture and HVR. (A) The C-domain architecture *in stereo*. The C_w- and C_h-domains are in gray and light green, respectively. The disulfide bridges and the residues forming the hydrophobic ridges are indicated. The HVR and its NCS counterpart are shown in red and blue, respectively. The variable loop (residues 539–549), flanked by two adjacent cysteine residues, is in green. (B) Crystal packing in the orthorhombic crystal. The crystallographically equivalent molecules (HVRs) are in cyan (blue) and pink (red), respectively. The arrows indicate the directions of the HVR chains. Zinc and calcium ions are represented as red and black spheres, respectively. (C) Interactions between the HVRs (cyan and pink) *in stereo*. The molecular surface of the cyan molecule is shown with the electrochemical surface potential (red to blue). The residues constituting the hydrophobic ridges are in yellow. The residues are labelled in blue and red for cyan and pink, respectively. (D) Water-mediated hydrogen-bond network in the HVR. The HVR residues are in pink and cyan; non-HVR residues in the pink molecule are in gray.

units through the C_h-domains such that the molecules form a handshake (Figure 4B). Each C_h-domain interacts with its counterpart through a relatively large complementary surface of 860 Å^2 forming another NCS at the center, although VAP1 exists as dimers, not as oligomers, and is mono-dispersed in solution (data not shown).

HVR as a potential adhesive interface

C_h-domain residues 562–583 are predominantly involved in the handshake (Figure 4B). This is the region in which the ADAM sequences are most divergent and variable in length (16–55 aa) (Figure 2 and Supplementary Figure 1). We have designated this as the hyper-variable region (HVR). The HVR

is subdivided into two structural elements. The N-terminal portion (residues 562–572) fits into an extended loop, filling the gap between the M-domain and the neighboring molecule's C_h-domain and thus fixing the position of the arm (Figure 4B). The variable structures and less-specific interactions suggest that this loop is stabilized by crystal packing. Some ADAMs possess a putative fusion peptide in this segment typical of viral fusion proteins (Blobel *et al*, 1992; Yagami-Hiromasa *et al*, 1995), although their role in the actual fusion process has not been demonstrated. However, the remainder of the HVR (residues 572–583) interacts extensively with its counterpart by forming an antiparallel β strand at the center (Figure 4C and D). Although the ability to form β strand is predictable from the sequence, this β strand is stabilized mainly by interchain interactions (Figure 4D). There are no intrachain hydrogen bonds between residues 574–577 and the remainder of the C_h-domain; however a water-mediated hydrogen-bond network stabilizes this segment (Figure 4D). Therefore, it appears, that this β strand might be formed by the induced-fit mechanism upon the association of the C_h-domains and that the conserved disulfide bond (Cys526–Cys572, see Figure 4D) may stabilize the structure when the HVRs are isolated in solution. In addition to the main-chain hydrogen bonds, side-chain atoms (particularly residues I574, Y575, Y576 and P578) in the HVR β strand contribute numerous von der Waals interactions with their counterparts. Aside from the HVR, aromatic residues located at both sides of the β strand in close proximity to the NCS axis create additional interaction surfaces: residues Phe515, Gly516, His535 and Tyr536 in the loop regions form hydrophobic ridges that fit complementarily into the NCS region (Figure 4C). The hydrophobic ridges are highly conserved among ADAMs (Figure 2 and Supplementary Figure 1), thus, in part, they may also constitute binding surfaces.

Discussion

The VAP1 structures reveal highly conserved structural calcium-binding sites and the numbers and the spacings of cysteinyl residues that are essential for maintaining structural rigidity and spatial arrangement of the ADAMs' MDC domains. The C-shaped MDC architecture implies meaningful interplay between the domains and their potential roles in physiological functions.

The HVR creates a novel interaction interface in collaboration with the conserved hydrophobic ridges. Different ADAMs have distinct HVR sequences, which result in distinct surface features, thus, they may function in specifying binding proteins. The HVR is at the distal end of the C-shaped arm and points toward the M-domain catalytic site, with a distance of ~4 nm in between them. Collectively, these observations suggest that the HVR captures the target or associated protein that is processed by the catalytic site (Figure 5). The disintegrin portion is located opposit to and apart from the catalytic site and, thus, might play a primary role as a scaffold that allocates these two functional units spatially. The C-shaped structure also implies how the ADAMs' C-domains cooperate with their M-domains (Reddy *et al*, 2000; Smith *et al*, 2002). In membrane-bound ADAMs, the EGF-like domain (~60 aa) follows the C_h-domain (Figure 2) and presumably works as a rigid spacer connecting the MDC-domains with and orientating against the membrane-spanning region (Figure 5A). Many ADAMs are proteolytically inactive (because of the defects in the catalytic HEXXHXXGXXHD sequence or the post-translational removal of the M-domain), and several of these are important developmentally. Therefore, the HVR may also work to modulate cell–cell and cell–matrix interactions. There is some experimental evidence for C-domain-mediated adhesion. Peptides encompassing the HVR and the hydrophobic ridge from P-III SVMPs interfere with platelet interaction and collagen binding (Kamiguti *et al*, 2003). A recombinant atrolysin-A C-domain specifically binds collagen I and von Willebrand factor (vWF) and blocks collagen–vWF interaction (Jia *et al*, 2000; Serrano *et al*, 2005). ADAM12 interacts with cell-surface syndecan through its C-domain and mediates integrin-dependent cell spreading (Iba *et al*, 2000). The D/C-domain portion of ADAM13 binds to the ECM proteins laminin and fibronectin (Gaultier *et al*, 2002). However, most of these studies do not assign specific regions of the C-domain to these interactions and the molecular recognition mechanisms are to be elucidated.

ADAM10 and ADAM17 lack the Ca^{2+}-binding site III and show less sequence similarities in the C-domain with other

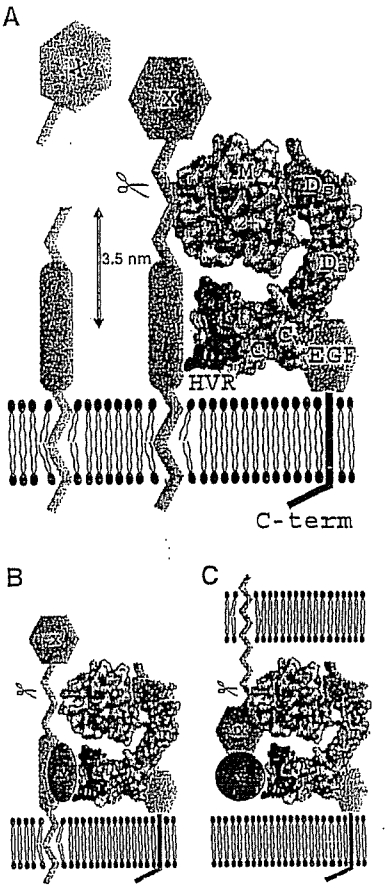

Figure 5 Models for ADAM's shedding. The molecular surface of the VAP1 monomer, without VAP1's unique H0-helix, are colored as in Figure 1A. Hydrophobic ridges are in yellow. EGF-like, transmembrane and cytoplasmic domains are represented schematically. (A) Membrane-anchored substrate molecule 'X' is directly recognized and captured by the HVR on the membrane-bound ADAM molecule. The distance between the center of the HVR (Tyr575) and the catalytic zinc ion is about 3.5 nm. (B) Substrate 'X' is recognized by the ADAM HVR via binding with an associated protein 'Y'. (C) ADAM cleaves substrate 'X' in *trans* via binding with an associated protein 'Y'.

canonical ADAMs (Supplementary Figure 1). Comparison of the recently solved ADAM10 D/C-domain partial structure ($ADAM10_{D+C}$) (Janes *et al*, 2005) and that of VAP1 reveals that the atypical ADAM10 shares the continuous D_a/C_w structure and the C_h-domain scaffold with VAP1; however, it has an disordered D_s-domain and an alternate HVR structure and a different orientation between C_w- and C_h-domains (Figure 6). The locations of four of the five disulfide bridges within the C_h-domain are conserved between VAP1 and ADAM10 (Figure 6B and C) and thus, they enabled us to align the two sequences (Figure 6E). Based on this alignment, we completed entire alignments (Supplementary Figure 1) including 38 sequences of mammalian ADAMs and *Schizosaccharomyces pombe* Mde10 (Nakamura *et al*, 2004), presumably the founding member of the ADAM family in evolutionary terms. The $ADAM10_{D+C}$ structure lacks the eight residues (583–590 in ADAM10) that may form a flexible loop. However, VAP1 (Figure 6E) and the canonical ADAMs except for ADAM8 (Supplementary Figure 1) have extra 16 residues in this segment that, in part, forms a variable loop, flanked by the adjacent cysteinyl residues (Cys539 and Cys549 in VAP1) and protrudes from the main body of the C-domain (Figures 4A and 6B). The variable loop has highest temperature factor in the molecule and resembles to the disintegrin-loop, thus can be an additional protein-binding interface. The six VAP1 monomer molecules represent almost the same C_w/C_h domain orientation (data not shown), however that is distinct from that of ADAM10 (Figure 5A). Thus, the possibility whether different ADAMs have distinct C_w/C_h domain orientation remains to be established. Janes *et al* (2005) have shown that the three glutamate residues outside of HVR are essential for ADAM10-mediated ephrin proteolysis in *trans*, however, roles of the ADAM10 HVR has not been examined. An extensive molecular surface of the elongated arm structure (12 000 Å^2 for the VAP1 D/C-domains) might reveal additional protein–protein interaction interfaces other than the HVR. Multiple charged residues in the D-domain are essential for ADAM28 binding to α4β1 (Bridges *et al*, 2003) and the RX_6DLPEF motif has been proposed for integrin α9β1 binding (Eto *et al*, 2002). However, the D-domain portion of the C-shaped scaffold is away from the catalytic site; thus, those additional sites might not directly serve as target recognition interfaces for catalysis.

Uniquely among cell-surface proteins, ADAMs display both proteolytic and adhesive activities. The VAP1 structure reveals that these functions are spatially allocated to the ends of the unique C-shaped scaffold and face each other. This spatial allocation of the functional sites provide us insights

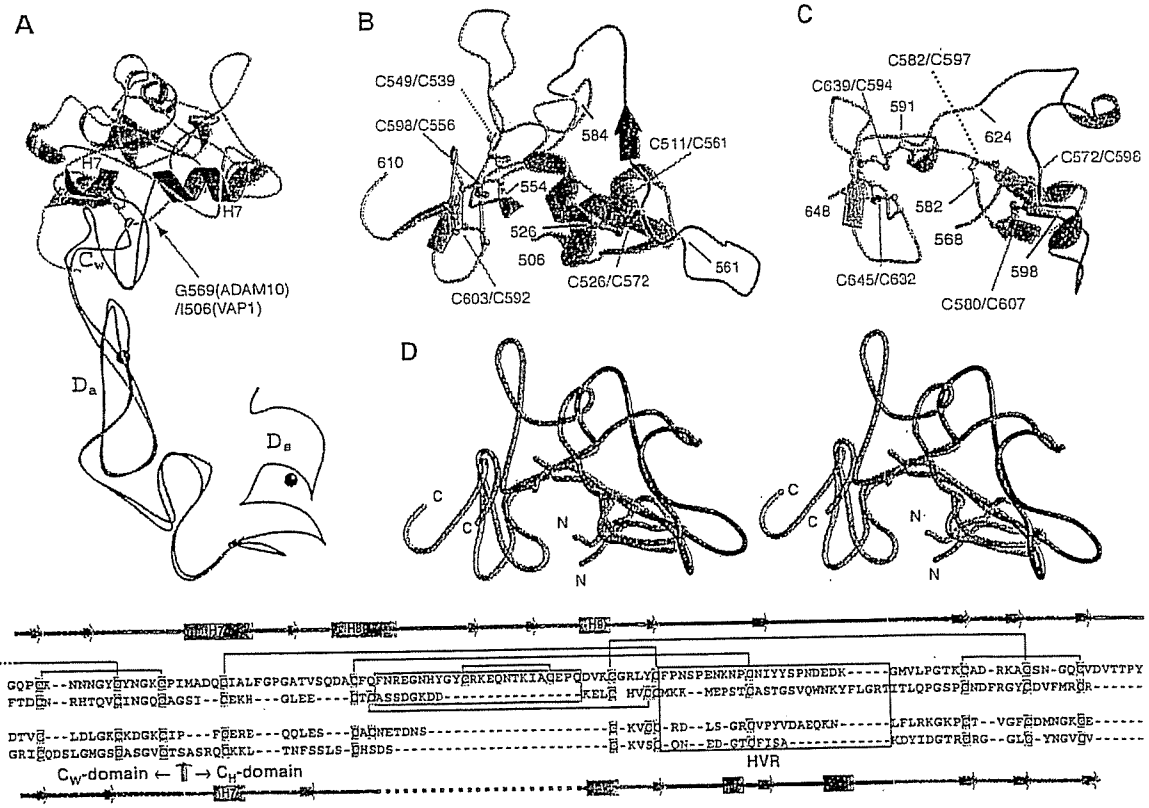

Figure 6 Comparison of the VAP1 and ADAM10 D/C domains. (A) Superimposition of the D_a-domains of ADAM10 and VAP1. The $D_s/D_a/C_w$-domains and the H7 helix of VAP1 and those of ADAM10 are shown in blue and red, respectively. The C_h-domains of VAP1 and ADAM10 are shown in cyan and pink, respectively. The arrow indicates the pivotal point between the C_w- and C_h-domains. Bound Ca^{2+} ions in VAP1 are shown as black spheres. (B) Ribbon representation of the C_h-domain of VAP1. The HVR is shown in blue. The common scaffold between the VAP1 and ADAM10 C_h-domains are shown in cyan and the segment lacking in ADAM10 is shown in light green. Disulfide bridges are indicated. (C) Ribbon representation of the C_h-domain of ADAM10. The HVR is shown in red. Disulfide brides are indicated. (D) Superimposition of the C_h-domains of VAP1 and ADAM10 *in stereo* with the colors as in (B, C). The N- and C-termini of the C_h-domains are indicated. (E) Structure-based alignments of VAP1, bovine ADAM10 (cADAM10), human ADAM17 (hADAM17) and *S. pombe* Mde10 (Mde10) C_w/C_h-domains. Secondary structures and the disulfide bridges are represented schematically. The HVR sequences and the missing segment in the ADAM10 structure are boxed in blue and green, respectively.

into the molecular mechanism of ADAMs' target recognition, which ADAMs shed which key substrates in specific biological events. Since ADAMs are potential therapeutic targets, the distinct surface feature created by the HVR of the individual ADAMs might also provide insights into the future design of drugs with higher specificity for each member of ADAMs. We suggest that the HVR, not the disintegrin domain, should be the focus of searches for physiological targets of ADAMs.

Materials and methods

Protein preparation and crystallization

The details of the preparation, crystallization and preliminary X-ray analysis of VAP1 will be described elsewhere (T Igarashi *et al*, in preparation). VAP1 was isolated from the crude snake *Crotalus atrox* venom (Sigma-Aldrich, USA) and subjected to sitting- or hanging-drop vapor diffusion crystallization. Two distinct crystal forms ($P2_12_12_1$ and $P4_12_12$) were obtained with the reservoir solution containing 15% polyethyleneglycol 8000 and 100 mM sodium cacodylate at pH 6.5, with (orthorhombic form) or without (tetragonal form) 20 mM cobaltous chloride hexahydrate. GM6001-bound crystals were prepared by adding GM6001 (CALBIOCHEM) to the drop with the orthorhombic crystal at a final concentration qof 0.33 mM (twice the protein concentration) followed by a 12-h incubation. Crystals were flash-frozen under the nitrogen flow at 90 K.

Diffraction data collection

All the diffraction data were collected at SPring-8 beamlines using either ADSC quantum 310R CCD (for the inhibitor-bound crystal at the beamline BL41XU with $\lambda = 1$ Å), Rigaku *R*-axis V imaging plate (for orthorhombic native crystal at the beamline BL45PX with $\lambda = 1$ Å) or Jupitor CCD (for the tetragonal crystal at the beamline BL45PX with $\lambda = 0.98$ Å) detectors at 90 K. The images were reduced using HKL2000. Both orthorhombic and tetragonal native data sets were collected to 2.5-Å resolution and inhibitor-bound crystal data sets were collected to 3.0 Å resolution (Table I).

Structural analysis

All structures were solved by the molecular replacement method by MOLREP in the CCP4 suite (CCP4, 1994) by using acutolysin-C (1QUA) (Zhu *et al*, 1999) as a starting model. Initially, the MR solution obtained from the orthorhombic crystal data set, assumed two M-domains in the asymmetric units. After manual rebuilding by TURBO-FRODO, the model was subjected to tortional molecular dynamic refinements with restrained NCS averaging of the M-domains using CNS (Brunger *et al*, 1998) and iterative refinements and manual rebuilding of the model improved the electron-density map and enabled us to extend the model. First, we found the electron densities associated with the pieces of helical segments of the molecules and modelled them as poly-alanine chains. After cycles of refinements, we assigned those segments as the parts of helices H7 and H8, where the secondary structures are predicted to be helices, judging from the electron densities associated with the side chains. At this stage, four tyrosine residues, Tyr575 and Try576 within the central β strands of the HVRs were clearly defined, and we noticed that there was another NCS-axis between the C-domains. After iterative rounds of refinements with restrained NCS averaging of the C-domains and manual model building, we completed modelling of the C-domains. From this stage onward, no NCS averaging was included in the refinements. Next, we modelled the D-domains with the help of automated chain tracing using the program ARP/wARP (Perrakis *et al*, 1999) and with the structural model of trimestatin (1J2L) as a guide. After completely modelling the polypeptide chains, we noticed that isolated lobes of high electron densities surrounded by oxygen atoms occurred both in the D_s- and D_a-domains. For these sites, calcium ions fit optimally to the electron density with a refined occupancy of 100% and reasonably low *B*-values, thus, we included calcium ions in the model. We also assigned a cobalt ion, which was supplemented in the crystallization buffer for the orthorhombic crystal form, located between the M- and D_s-domains in the A molecule. The part of the carbohydrate chain linked to residue Asn218 (two *N*-acetylglocosamine (NAG) moieties) was modelled. Then, water molecules were assigned. The *VAP1* cDNA encodes a protein with 610 amino-acid residues; however, the N-terminus is processed by post-translational modification (Masuda *et al*, 1998, 2000). Here, protein sequencing of the de-blocked VAP1 molecule clarified that the Glu184 side chain was modified into a pyro-form. The electron densities associated with almost the entire molecule except for the first pyroglutamic acid were defined in either monomer within the orthorhombic crystal. In the final model, 86.1% of the residues lay in the most favorable region, 13.3% in the additionally allowed region and 0.7% in the generously allowed region of the Ramachandran plot. The tetragonal crystal and inhibitor-bound crystal were solved by MR with the domains of the refined orthorhombic apo-form as a starting model. In the final model, 83.6% (80.6%) of the residues lay in the most favorable region, 15.7% (18.9%) in the additionally allowed region and 0.7% (0.5%) in the generously allowed region for tetragonal (inhibitor-bound) crystals in the Ramachandran plot. In either crystal form, the asymmetric unit contained one dimer molecule. All six monomers had almost identical structures. Refinement statistics are shown in Table I.

PDB accession codes

Atomic coordinates and structure factors have been deposited in the Protein Data Bank under accession codes 2ERO, 2ERP and 2ERQ for the orthorhombic native, GM6001-bound form and tetragonal-form, respectively.

Supplementary data

Supplementary data are available at *The EMBO Journal* Online.

Acknowledgements

We thank Yuko Oishi and staff in SPring-8 beamlines for assistance with data acquisition and Junichi Takagi for discussions and critical reading of the manuscript. This work was partly supported by Grant nano-001 for Research on Advanced Medical Technology from the Ministry of Health, Labor, and Welfare of Japan, and by grants from the Takeda Science Foundation, from the Kao Foundation for Arts and Science and from Senri Life Science Foundation. The authors declare no competing financial interests.

References

Almeida EA, Huovila AP, Sutherland AE, Stephens LE, Calarco PG, Shaw LM, Mercurio AM, Sonnenberg A, Primakoff P, Myles DG, White JM (1995) Mouse egg integrin alpha 6 beta 1 functions as a sperm receptor. *Cell* 81: 1095–1104

Becherer JD, Blobel CP (2003) Biochemical properties and functions of membrane-anchored metalloprotease-disintegrin proteins (ADAMs). *Curr Top Dev Biol* 54: 101–123

Black RA, Rauch CT, Kozlosky CJ, Peschon JJ, Slack JL, Wolfson MF, Castner BJ, Stocking KL, Reddy P, Srinivasan S, Nelson N, Boiani N, Schooley KA, Gerhart M, Davis R, Fitzner JN, Johnson RS, Paxton RJ, March CJ, Cerretti DP (1997) A metalloproteinase disintegrin that releases tumour-necrosis factor-alpha from cells. *Nature* 385: 729–733

Blobel CP (2005) ADAMs: key components in EGFR signalling and development. *Nat Rev Mol Cell Biol* 6: 32–43

Blobel CP, Myles DG, Primakoff P, White JM (1990) Proteolytic processing of a protein involved in sperm-egg fusion correlates with acquisition of fertilization competence. *J Cell Biol* 111: 69–78

Blobel CP, Wolfsberg TG, Turck CW, Myles DG, Primakoff P, White JM (1992) A potential fusion peptide and an integrin ligand domain in a protein active in sperm-egg fusion. *Nature* 356: 248–252

Bode W, Gomis-Ruth FX, Stockler W (1993) Astacins, serralysins, snake venom and matrix metalloproteinases exhibit identical zinc-binding environments (HEXXHXXGXXH and Met-turn) and

topologies and should be grouped into a common family, the 'metzincins'. *FEBS Lett* 331: 134–140

Bridges LC, Hanson KR, Tani PH, Mather T, Bowditch RD (2003) Integrin alpha4beta1-dependent adhesion to ADAM 28 (MDC-L) requires an extended surface of the disintegrin domain. *Biochemistry* 42: 3734–3741

Brunger AT, Adams PD, Clore GM, DeLano WL, Gros P, Grosse-Kunstleve RW, Jiang JS, Kuszewski J, Nilges M, Pannu NS, Read RJ, Rice LM, Simonson T, Warren GL (1998) Crystallography & NMR system: a new software suite for macromolecular structure determination. *Acta Crystallogr D* 54 (Part 5): 905–921

Calvete JJ, Marcinkiewicz C, Monleon D, Esteve V, Celda B, Juarez P, Sanz L (2005) Snake venom disintegrins: evolution of structure and function. *Toxicon* 45: 1063–1074

CCP4 (1994) The CCP4 suite: programs for protein crystallography. *Acta Crystallogr D* 50: 760–763

Duffy MJ, Lynn DJ, Lloyd AT, O'Shea CM (2003) The ADAMs family of proteins: from basic studies to potential clinical applications. *Thromb Haemost* 89: 622–631

Eto K, Huet C, Tarui T, Kupriyanov S, Liu HZ, Puzon-McLaughlin W, Zhang XP, Sheppard D, Engvall E, Takada Y (2002) Functional classification of ADAMs based on a conserved motif for binding to integrin alpha 9beta 1: implications for sperm-egg binding and other cell interactions. *J Biol Chem* 277: 17804–17810

Evans JP (2001) Fertilin beta and other ADAMs as integrin ligands: insights into cell adhesion and fertilization. *BioEssays* 23: 628–639

Fox JW, Serrano SM (2005) Structural considerations of the snake venom metalloproteinases, key members of the M12 reprolysin family of metalloproteinases. *Toxicon* 45: 969–985

Fujii Y, Okuda D, Fujimoto Z, Horii K, Morita T, Mizuno H (2003) Crystal structure of trimestatin, a disintegrin containing a cell adhesion recognition motif RGD. *J Mol Biol* 332: 1115–1122

Gaultier A, Cousin H, Darribere T, Alfandari D (2002) ADAM13 disintegrin and cysteine-rich domains bind to the second heparin-binding domain of fibronectin. *J Biol Chem* 277: 23336–23344

Huang TF, Holt JC, Lukasiewicz H, Niewiarowski S (1987) Trigramin. A low molecular weight peptide inhibiting fibrinogen interaction with platelet receptors expressed on glycoprotein IIb–IIIa complex. *J Biol Chem* 262: 16157–16163

Iba K, Albrechtsen R, Gilpin B, Frohlich C, Loechel F, Zolkiewska A, Ishiguro K, Kojima T, Liu W, Langford JK, Sanderson RD, Brakebusch C, Fassler R, Wewer UM (2000) The cysteine-rich domain of human ADAM 12 supports cell adhesion through syndecans and triggers signaling events that lead to beta1 integrin-dependent cell spreading. *J Cell Biol* 149: 1143–1156

Janes PW, Saha N, Barton WA, Kolev MV, Wimmer-Kleikamp SH, Nievergall E, Blobel CP, Himanen JP, Lackmann M, Nikolov DB (2005) Adam meets Eph: an ADAM substrate recognition module acts as a molecular SWITCH for Ephrin cleavage *in trans*. *Cell* 123: 291–304

Jia LG, Shimokawa K, Bjarnason JB, Fox JW (1996) Snake venom metalloproteinases: structure, function and relationship to the ADAMs family of proteins. *Toxicon* 34: 1269–1276

Jia LG, Wang XM, Shannon JD, Bjarnason JB, Fox JW (2000) Inhibition of platelet aggregation by the recombinant cysteine-rich domain of the hemorrhagic snake venom metalloproteinase, atrolysin A. *Arch Biochem Biophys* 373: 281–286

Kamiguti AS, Gallagher P, Marcinkiewicz C, Theakston RD, Zuzel M, Fox JW (2003) Identification of sites in the cysteine-rich domain of the class P-III snake venom metalloproteinases responsible for inhibition of platelet function. *FEBS Lett* 549: 129–134

Maskos K, Fernandez-Catalan C, Huber R, Bourenkov GP, Bartunik H, Ellestad GA, Reddy P, Wolfson MF, Rauch CT, Castner BJ, Davis R, Clarke HR, Petersen M, Fitzner JN, Cerretti DP, March CJ, Paxton RJ, Black RA, Bode W (1998) Crystal structure of the catalytic domain of human tumor necrosis factor-alpha-converting enzyme. *Proc Natl Acad Sci USA* 95: 3408–3412

Masuda S, Hayashi H, Araki S (1998) Two vascular apoptosis-inducing proteins from snake venom are members of the metalloprotease/disintegrin family. *Eur J Biochem* 253: 36–41

Masuda S, Ohta T, Kaji K, Fox JW, Hayashi H, Araki S (2000) cDNA cloning and characterization of vascular apoptosis-inducing protein 1. *Biochem Biophys Res Commun* 278: 197–204

Moss ML, Bartsch JW (2004) Therapeutic benefits from targeting of ADAM family members. *Biochemistry* 43: 7227–7235

Moss ML, Jin SL, Milla ME, Bickett DM, Burkhart W, Carter HL, Chen WJ, Clay WC, Didsbury JR, Hassler D, Hoffman CR, Kost TA, Lambert MH, Leesnitzer MA, McCauley P, McGeehan G, Mitchell J, Moyer M, Pahel G, Rocque W, Overton LK, Schoenen F, Seaton T, Su JL, Warner J, Willard D, Becherer JD (1997) Cloning of a disintegrin metalloproteinase that processes precursor tumour-necrosis factor-alpha. *Nature* 385: 733–736

Myles DG, Kimmel LH, Blobel CP, White JM, Primakoff P (1994) Identification of a binding site in the disintegrin domain of fertilin required for sperm-egg fusion. *Proc Natl Acad Sci USA* 91: 4195–4198

Nakamura T, Abe H, Hirata A, Shimoda C (2004) ADAM family protein Mde10 is essential for development of spore envelopes in the fission yeast *Schizosaccharomyces pombe*. *Eukaryot Cell* 3: 27–39

Orth P, Reichert P, Wang W, Prosise WW, Yarosh-Tomaine T, Hammond G, Ingram RN, Xiao L, Mirza UA, Zou J, Strickland C, Taremi SS, Le HV, Madison V (2004) Crystal structure of the catalytic domain of human ADAM33. *J Mol Biol* 335: 129–137

Pan D, Rubin GM (1997) Kuzbanian controls proteolytic processing of Notch and mediates lateral inhibition during *Drosophila* and vertebrate neurogenesis. *Cell* 90: 271–280

Perrakis A, Morris R, Lamzin VS (1999) Automated protein model building combined with iterative structure refinement. *Nat Struct Biol* 6: 458–463

Primakoff P, Hyatt H, Tredick-Kline J (1987) Identification and purification of a sperm surface protein with a potential role in sperm-egg membrane fusion. *J Cell Biol* 104: 141–149

Qi H, Rand MD, Wu X, Sestan N, Wang W, Rakic P, Xu T, Artavanis-Tsakonas S (1999) Processing of the notch ligand delta by the metalloprotease Kuzbanian. *Science* 283: 91–94

Reddy P, Slack JL, Davis R, Cerretti DP, Kozlosky CJ, Blanton RA, Shows D, Peschon JJ, Black RA (2000) Functional analysis of the domain structure of tumor necrosis factor-alpha converting enzyme. *J Biol Chem* 275: 14608–14614

Rooke J, Pan D, Xu T, Rubin GM (1996) KUZ, a conserved metalloprotease-disintegrin protein with two roles in *Drosophila* neurogenesis. *Science* 273: 1227–1231

Seals DF, Courtneidge SA (2003) The ADAMs family of metalloproteases: multidomain proteins with multiple functions. *Genes Dev* 17: 7–30

Serrano SM, Jia LG, Wang D, Shannon JD, Fox JW (2005) Function of the cysteine-rich domain of the haemorrhagic metalloproteinase atrolysin A: targeting adhesion proteins collagen I and von Willebrand factor. *Biochem J* 391: 69–76

Smith KM, Gaultier A, Cousin H, Alfandari D, White JM, DeSimone DW (2002) The cysteine-rich domain regulates ADAM protease function *in vivo*. *J Cell Biol* 159: 893–902

Van Eerdewegh P, Little RD, Dupuis J, Del Mastro RG, Falls K, Simon J, Torrey D, Pandit S, McKenny J, Braunschweiger K, Walsh A, Liu Z, Hayward B, Folz C, Manning SP, Bawa A, Saracino L, Thackston M, Benchekroun Y, Capparell N, Wang M, Adair R, Feng Y, Dubois J, FitzGerald MG, Huang H, Gibson R, Allen KM, Pedan A, Danzig MR, Umland SP, Egan RW, Cuss FM, Rorke S, Clough JB, Holloway JW, Holgate ST, Keith TP (2002) Association of the ADAM33 gene with asthma and bronchial hyperresponsiveness. *Nature* 418: 426–430

White JM (2003) ADAMs: modulators of cell–cell and cell–matrix interactions. *Curr Opin Cell Biol* 15: 598–606

Yagami-Hiromasa T, Sato T, Kurisaki T, Kamijo K, Nabeshima Y, Fujisawa-Sehara A (1995) A metalloprotease-disintegrin participating in myoblast fusion. *Nature* 377: 652–656

Zhu X, Teng M, Niu L (1999) Structure of acutolysin-C, a haemorrhagic toxin from the venom of Agkistrodon acutus, providing further evidence for the mechanism of the pH-dependent proteolytic reaction of zinc metalloproteinases. *Acta Crystallogr D* 55: 1834–1841

Zolkiewska A (1999) Disintegrin-like/cysteine-rich region of ADAM 12 is an active cell adhesion domain. *Exp Cell Res* 252: 423–431

Am J Physiol Heart Circ Physiol 291: H1138–H1146, 2006.
First published April 28, 2006; doi:10.1152/ajpheart.00187.2006.

Cardioprotective role of endogenous hydrogen peroxide during ischemia-reperfusion injury in canine coronary microcirculation in vivo

Toyotaka Yada,[1] Hiroaki Shimokawa,[3] Osamu Hiramatsu,[1] Yoshisuke Haruna,[2] Yoshitaka Morita,[2] Naoki Kashihara,[2] Yoshiro Shinozaki,[4] Hidezo Mori,[5] Masami Goto,[1] Yasuo Ogasawara,[1] and Fumihiko Kajiya[1]

[1]*Department of Medical Engineering and Systems Cardiology and* [2]*Division of Nephrology and Rheumatology, Department of Internal Medicine, Kawasaki Medical School, Kurashiki;* [3]*Department of Cardiovascular Medicine, Tohoku University Graduate School of Medicine, Sendai;* [4]*Department of Physiology, Tokai University School of Medicine, Isehara; and* [5]*Department of Cardiac Physiology, National Cardiovascular Center Research Institute, Suita, Japan*

Submitted 22 February 2006; accepted in final form 18 April 2006

Yada, Toyotaka, Hiroaki Shimokawa, Osamu Hiramatsu, Yoshisuke Haruna, Yoshitaka Morita, Naoki Kashihara, Yoshiro Shinozaki, Hidezo Mori, Masami Goto, Yasuo Ogasawara, and Fumihiko Kajiya. Cardioprotective role of endogenous hydrogen peroxide during ischemia-reperfusion injury in canine coronary microcirculation in vivo. *Am J Physiol Heart Circ Physiol* 291: H1138–H1146, 2006. First published April 28, 2006; doi:10.1152/ajpheart.00187.2006.—We have recently demonstrated that endogenous H_2O_2 plays an important role in coronary autoregulation in vivo. However, the role of H_2O_2 during coronary ischemia-reperfusion (I/R) injury remains to be examined. In this study, we examined whether endogenous H_2O_2 also plays a protective role in coronary I/R injury in dogs in vivo. Canine subepicardial small coronary arteries (≥100 μm) and arterioles (<100 μm) were continuously observed by an intravital microscope during coronary I/R (90/60 min) under cyclooxygenase blockade (n = 50). Coronary vascular responses to endothelium-dependent vasodilators (ACh) were examined before and after I/R under the following seven conditions: control, nitric oxide (NO) synthase (NOS) inhibitor N^G-monomethyl-L-arginine (L-NMMA), catalase (a decomposer of H_2O_2), 8-sulfophenyltheophylline (8-SPT, an adenosine receptor blocker), L-NMMA + catalase, L-NMMA + tetraethylammonium (TEA, an inhibitor of large-conductance Ca^{2+}-sensitive potassium channels), and L-NMMA + catalase + 8-SPT. Coronary I/R significantly impaired the coronary vasodilatation to ACh in both sized arteries (both $P < 0.01$); L-NMMA reduced the small arterial vasodilatation (both $P < 0.01$), whereas it increased ($P < 0.05$) the ACh-induced coronary arteriolar vasodilatation associated with fluorescent H_2O_2 production after I/R. Catalase increased the small arterial vasodilatation ($P < 0.01$) associated with fluorescent NO production and increased endothelial NOS expression, whereas it decreased the arteriolar response after I/R ($P < 0.01$). L-NMMA + catalase, L-NMMA + TEA, or L-NMMA + catalase + 8-SPT further decreased the coronary vasodilatation in both sized arteries (both, $P < 0.01$). L-NMMA + catalase, L-NMMA + TEA, and L-NMMA + catalase + 8-SPT significantly increased myocardial infarct area compared with the other four groups (control, L-NMMA, catalase, and 8-SPT; all, $P < 0.01$). These results indicate that endogenous H_2O_2, in cooperation with NO, plays an important cardioprotective role in coronary I/R injury in vivo.

endothelium-derived relaxing factor; myocardial infarction; vascular endothelial function

VASCULAR ENDOTHELIAL CELLS play an important role in maintaining vascular homeostasis by synthesizing and releasing endothelium-derived relaxing factors (EDRFs), including prostacyclin (PGI_2), nitric oxide (NO), and endothelium-derived hyperpolarizing factor (EDHF) (6, 9, 26). Endothelial dysfunction is thus characterized by a reduction in the activity of PGI_2, NO, and EDHF, thereby enhancing vasoconstrictor responses mediated by endothelin, serotonin, and thrombin (26). Endothelial injury secondary to myocardial ischemia-reperfusion (I/R) decreases the production and activity of EDRFs in acute myocardial infarction (18).

Among the three different EDRFs, the roles of PGI_2 and NO have been extensively investigated (6, 9, 26). Regarding EDHF, since the first reports on its existence (6, 9), several candidates for EDHF have been proposed, including cytochrome *P*-450 metabolites (2, 4), endothelium-derived K^+ (7), and electrical communications through gap junctions between endothelial cells and vascular smooth muscle cells (29). Matoba et al. (16, 17) have previously identified that endothelium-derived H_2O_2 is a primary EDHF in mesenteric arteries of mice and humans. Morikawa et al. (21) have recently confirmed that endothelial Cu,Zn-SOD plays an important role as an EDHF synthase in mice. We have subsequently confirmed the importance of H_2O_2 in canine coronary microcirculation during coronary autoregulation with reduced coronary perfusion pressure in vivo (35).

However, it remains to be examined whether H_2O_2 also exerts cardioprotective effects during I/R in the coronary microcirculation in vivo, and if so, whether such effects of H_2O_2 compensate the impaired NO-mediated responses due to I/R injury in vivo. In this study, we tested our hypothesis that H_2O_2 plays an important cardioprotective and compensatory role during coronary I/R injury in dogs in vivo.

METHODS

This study conformed to the Guideline on Animal Experiments of Kawasaki Medical School, and approved by an independent review committee from the same institution, and the *Guide for the Care and Use of Laboratory Animals* published by the National Institutes of Health.

Animal preparation. Anesthetized mongrel dogs (15–25 kg in body wt, n = 50) of either sex were ventilated with a ventilator (model VS600, IDC, Pittsburgh, PA). Aortic pressure and left ventricular (LV) pressure were continuously monitored with a catheter (SPC-784A, Millar, TX). The blood flow of the left anterior descending coronary artery (LAD) was continuously measured by a transonic flow probe (T206, Transonic Systems, Ithaca, NY).

Address for reprint requests and other correspondence: T. Yada, Dept. of Medical Engineering and Systems Cardiology, Kawasaki Medical School, 577 Matsushima, Kurashiki, Okayama 701-0192, Japan (e-mail: yada@me.kawasaki-m.ac.jp).

The costs of publication of this article were defrayed in part by the payment of page charges. The article must therefore be hereby marked "*advertisement*" in accordance with 18 U.S.C. Section 1734 solely to indicate this fact.

Measurements of coronary diameter by intravital microscope. We continuously monitored coronary vascular responses by an intravital microscope (VMS 1210, Nihon-Kohden, Tokyo) with a needle probe in vivo as previously described (32). We gently placed the needle probe on subepicardial microvessels. When a clear vascular image was obtained, end-diastolic vascular images were taken with 30 pictures/s (32).

Measurements of regional myocardial blood flow. Regional myocardial blood flow was measured by the nonradioactive microsphere (Sekisui Plastic, Tokyo) technique, as previously described (20). Briefly, the microsphere suspension was injected into the left atrium 85 min after the onset of coronary occlusion. Myocardial collateral flow in the apex during suturing of the collateral vessels from the left circumflex artery (LCX) was calculated according to the formula: time flow = tissue counts × (reference flow/reference counts) and was expressed in milliliters per gram per minute (20).

Detection of H_2O_2 and NO production. 2′,7′-Dichlorodihydrofluorescein diacetate (DCF, Molecular Probes, Eugene, OR) and diaminorhodamine-4M AM (DAR, Daiichi Pure Chemicals, Tokyo) were used to detect H_2O_2 and NO production in coronary microvessels without a different NO scavenger (e.g., methylene blue), respectively, as previously described (21). Briefly, fresh and unfixed heart tissue was cut into several blocks and frozen in optimal cutting temperature compound (Tissue-Tek, Sakura Fine Chemical, Tokyo) within a few hours. Fluorescent images of [illegible] after application of ACh by using [illegible] pus BX51, Tokyo) (21). We used different animals for the [illegible] treatment (DCF and DAR) and the 2,3,5-triphenyltetrazolium chloride (TTC) treatment.

Western blotting. Portions of myocardial samples were homogenized in lysis buffer. After centrifugation, the supernatants were used for Western immunoblotting. The proteins were transferred by semi-dry electroblotting to polyvinylidene difluoride membranes. The blots were then blocked and incubated with horseradish peroxidase-conjugated rabbit anti-endothelial NO synthase (eNOS, dimer form) polyclonal antibody (Santa Cruz Biotechnology, Santa Cruz, CA) or anti-actin antibody (Santa Cruz Biotechnology). The antibody was visualized by using an enhanced chemiluminescence method (ECL; Amersham Biosciences, Tokyo). The integrated density of the bands was quantified by using NIH Image analysis, and the protein expression level of eNOS was normalized to that of actin (24).

Experimental protocols. After the surgical procedure and instrumentation, at least 30 min was allowed for stabilization while hemodynamic variables were monitored. The following protocols were examined.

Coronary vascular responses to endothelium-dependent [ACh, 0.5 and 1.0 μg/kg intracoronary (ic)] and -independent [sodium nitroprusside (SNP), 40 and 80 μg/min ic] vasodilators were examined before ischemia (90 min)-reperfusion (60 min) (I/R). ACh and SNP were continuously and retrogradely infused into the diagonal branch of the LAD by using a syringe pump (STC 525, Terumo, Tokyo). The coronary vascular responses to ACh and SNP were examined for 2 min, and the image of maximal vasodilatation was taken at 2 min of infusion of ACh or SNP.

Coronary vasodilator responses to ACh and SNP were examined before and after coronary ischemia (90 min)-reperfusion (60 min) by proximal LAD occlusion under the following seven conditions with cyclooxygenase blockade (ibuprofen, 12.5 mg/kg iv) to evaluate the [illegible] and NO without PGI_2 in a different set of animals (Fig. [illegible] arginine (L-NMMA) [illegible] and 240,000 U·kg [illegible] H_2O_2 into water and oxygen), *4*) adenosine receptor blockade alone [8-sulfophenyltheophylline (8-SPT), 25 $\mu g \cdot kg^{-1} \cdot min^{-1}$ ic for 5 min], *5*) catalase plus L-NMMA, *6*) catalase plus tetraethylammonium [TEA, 10 $\mu g \cdot kg^{-1} \cdot min^{-1}$ ic for 10 min, an inhibitor of large-

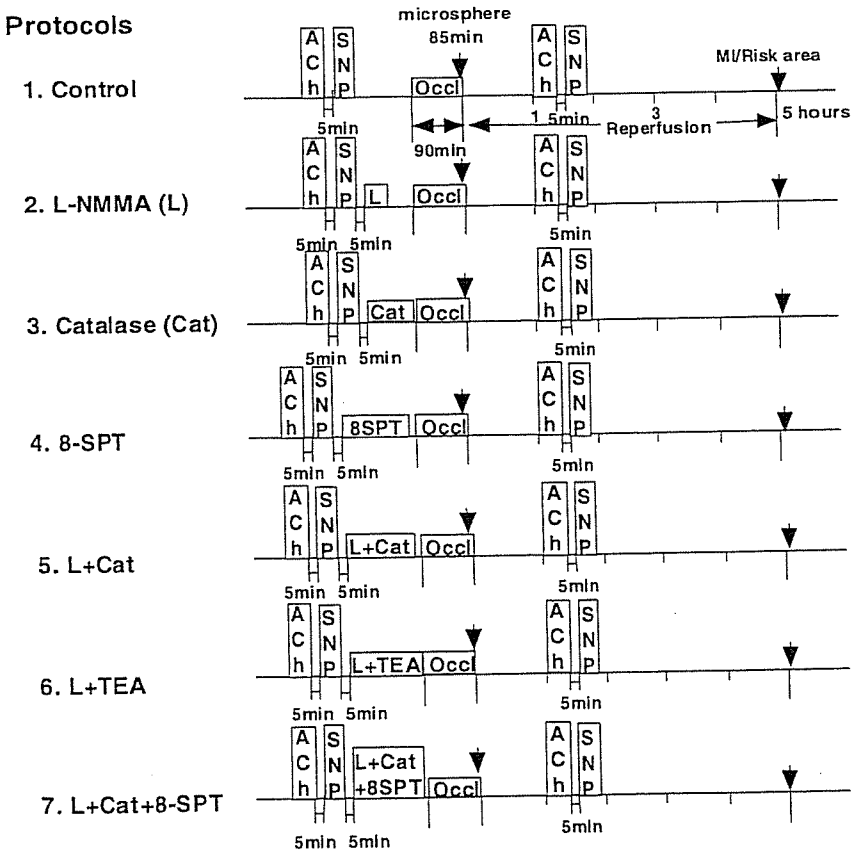

Fig. 1. Experimental protocols. TEA, tetraethylammonium; 8-SPT, 8-sulfophenyltheophylline; ACh, acetylcholine; SNP, sodium nitroprusside; Occl, coronary occlusion; Cat, catalase; L-NMMA (L), N^G-monomethyl-L-arginine; MI, myocardial infarction.

Table 1. *Hemodynamics during coronary ischemia-reperfusion injury in dogs*

		Before I/R			Ischemia (85 min)	After I/R		
	n	Baseline	ACh	SNP		Baseline	ACh	SNP
MBP, mmHg								
Control	5	92±4	91±6	92±5	93±14	92±4	91±5	92±6
L-NMMA	5	97±8	98±7	94±9	92±10	97±7	98±8	95±8
Cat	5	96±8	92±8	94±9	92±9	96±7	96±8	98±6
L-NMMA + Cat	5	94±4	93±9	97±9	95±11	95±8	98±5	94±5
L-NMMA + TEA	5	95±12	93±13	95±14	94±10	91±14	93±15	98±10
L-NMMA + Cat + 8-SPT	5	95±3	96±4	95±3	93±11	96±3	97±4	95±3
Heart rate, beats/min								
Control	5	152±5	155±3	154±3	156±7	156±5	154±5	153±5
L-NMMA	5	157±5	156±5	157±6	158±6	153±5	153±5	153±5
Cat	5	155±4	159±6	158±5	157±6	151±7	155±8	154±8
L-NMMA + Cat	5	156±12	158±13	158±13	154±5	156±13	156±14	159±13
L-NMMA + TEA	5	153±13	154±12	155±11	155±5	150±10	151±11	152±10
L-NMMA + Cat + 8-SPT	5	152±7	155±9	153±3	153±5	152±7	151±6	153±7

Results are expressed as means ± SE; *n* = no. of dogs. I/R, ischemia-reperfusion; MBP, mean blood pressure; Cat, catalase; SNP, sodium nitroprusside; TEA, tetraethylammonium; 8-SPT, sulfophenyltheophylline; L-NMMA, N^G-monomethyl-L-arginine.

conductance Ca^{2+}-sensitive potassium (K_{Ca}) channels], and 7) catalase plus L-NMMA with 8-SPT (35). These inhibitors were given at 30 min before I/R. An interval between each treatment was 5 min. The basal coronary diameter was defined as that before administration of ACh or SNP either before or after I/R. L-NMMA, catalase, TEA, and 8-SPT were administered alone at 5 min after administration of ACh or SNP. Microspheres were administered at 85 min after the initiation of coronary occlusion. In the combined infusion (L-NMMA + catalase + 8-SPT), catalase solution was infused into the LAD at a rate of 0.5 ml/min at 5 min after infusion of L-NMMA, and then 8-SPT was added into the LAD at 15 min after the initiation of L-NMMA.

After 1 h of reperfusion, coronary vasodilator responses to ACh and SNP were examined.

After 5 h of reperfusion, we reoccluded the LAD and injected Evans blue dye into a systemic vein. Then, myocardial slices (5 μm thick) were incubated in 1% TTC (Sigma) solution to detect the infarct area (36). Different animals were used for fluorescent treatment (DCF and DAR) and TTC treatment.

Drugs. All drugs were obtained from Sigma Chemical and were diluted in a physiological saline immediately before use.

Statistical analysis. Results are expressed as means ± SE. Vascular responses (see Figs. 3*C*, 5*F*, 6*F*, 7, and 9*A*) were analyzed by one-way ANOVA followed by Scheffé's post hoc test for multiple comparisons. Difference in the effects of ACh and SNP on subepicardial coronary microvessels before and after I/R (see Figs. 3, *A* and *B*, 4, and 8, *A* and *B*), and difference between infarct size/risk area and transmural collateral flow in control and other inhibitors (see Fig. 9*B*) were examined by a multiple regression analysis by using a model in which the change in coronary diameter was set as a dependent variable (y) and vascular size as an explanatory variable (x), while the statuses of control and other inhibitors were set as dummy variables (D_1, D_2) in the following equation: $y = a_0 + a_1x + a_2D_1 + a_3D_2$, where a_0 through a_3 are partial regression coefficients (36). The criterion for statistical significance was at $P < 0.05$.

RESULTS

Hemodynamics and blood gases during I/R injury. Immediately after reperfusion, coronary blood flow was increased and some arrhythmias occurred; however, those changes returned to the control levels 1 h after reperfusion when we repeated the measurements. Thus, throughout the experiments, mean aortic pressure and heart rate at baseline were constant and comparable, and Po_2, Pco_2, and pH were maintained within the physiological ranges (pH 7.35–7.45, Po_2 > 70 mmHg, and Pco_2 25–40 mmHg,). Hemodynamic variables at baseline did not significantly change after I/R compared with those before I/R (Tables 1 and 2).

Dose responses to ACh and SNP. ACh (0.5 and 1.0 μg/kg ic) and SNP (40 and 80 μg/min ic) caused coronary vasodilatation in a dose-dependent manner at both small arteries and arterioles (Fig. 2). Then we chose the maximal dose of the vasodilators (ACh, 1.0 μg/kg ic, and SNP, 80 μg/min ic) in the following experiments.

Endothelium-dependent coronary vasodilatation before and after I/R. There was no significant difference in baseline diameter after ACh before I/R among the groups. All inhibitors did not affect resting coronary artery diameter or coronary

Table 2. *Baseline vascular diameter before I/R in response to ACh*

	Small Artery	Arteriole
Control	104–150 μm (120±7, *n* = 7)	37–96 μm (70±6, *n* = 12)
L-NMMA	106–164 μm (131±7, *n* = 8)	36–95 μm (63±5, *n* = 16)
Cat	100–147 μm (121±5, *n* = 10)	28–89 μm (61±6, *n* = 12)
8-SPT	114–162 μm (130±8, *n* = 6)	30–88 μm (60±10, *n* = 5)
L-NMMA + Cat	102–141 μm (118±5, *n* = 8)	34–95 μm (77±4, *n* = 10)
L-NMMA + TEA	105–142 μm (123±6, *n* = 5)	34–95 μm (62±9, *n* = 8)
L-NMMA + Cat + 8-SPT	110–145 μm (128±6, *n* = 5)	38–87 μm (67±7, *n* = 7)

Results are expressed as range (means ± SE); *n* = no. of blood vessels.

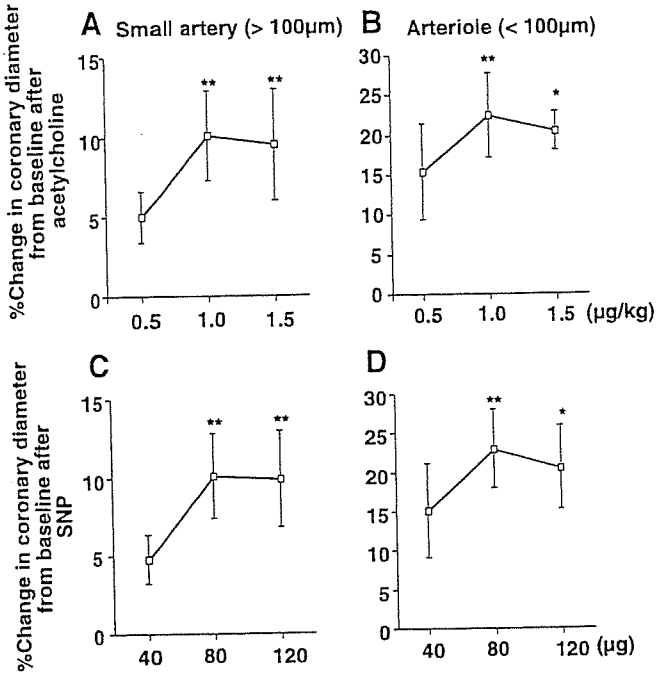

Fig. 2. Dose responses to ACh (*A* and *B*) and SNP (*C* and *D*) before ischemia-reperfusion (I/R). Number of small arteries (*A* and *C*) and arterioles (*B* and *D*) per animals used was 5/5 for each group. $*P < 0.05$, $**P < 0.01$ vs. ACh (0.5 μg/kg) and SNP (40 μg).

blood flow. Under control conditions (before I/R), intracoronary administration of ACh caused a significantly greater coronary vasodilatation in arterioles than in small arteries (Fig. 3, *A* and *B*). Coronary I/R significantly impaired the coronary vasodilatation to ACh in both sized arteries (Figs. 3*A* and 4*A*), and L-NMMA reduced the vasodilatation in small arteries (Figs. 3*A* and 4*B*) but rather increased the response in arterioles compared with control (Figs. 3*B* and 4*A*) after I/R. Catalase and 8-SPT increased the ACh-induced vasodilatation in small arteries (Figs. 3*A* and 4, *C* and *D*) but decreased the response in arterioles (Fig. 3*B*) after I/R. There was no significant difference in coronary blood flow before and after I/R among the control, the L-NMMA, and the catalase group (Fig. 3*C*). L-NMMA + catalase (Figs. 3, *A* and *B*, and 4*E*) or L-NMMA + TEA (Figs. 3, *A* and *B*, and 4*F*) decreased the vasodilatation in both sized arteries (Fig. 3, *A* and *B*) with decrement of coronary blood flow (Fig. 3*C*), and L-NMMA plus catalase with 8-SPT further decreased the vasodilatation in both sized arteries (Figs. 3, *A* and *B*, and 4*G*) compared with other groups (Fig. 3, *A–C*).

Detection of H_2O_2 and NO production. Fluorescent microscopy with DCF showed that I/R increased the vascular H_2O_2 production in control LCX (Fig. 5, *B* and *F*) compared with baseline conditions (Fig. 5, *A* and *F*) and decreased the H_2O_2 production in control LAD (Figs. 5, *C* and *F*), which was enhanced by L-NMMA (Fig. 5, *D* and *F*) and was abolished by catalase (Fig. 5, *E* and *F*) in arterioles. By contrast, the production of NO as assessed with DAR fluorescence was increased in control LCX (Fig. 6, *B* and *F*) compared with baseline LCX (Fig. 6, *A* and *F*) after I/R, decreased in control LAD (Fig. 6, *C* and *F*), inhibited by L-NMMA (Fig. 6, *D* and *F*), and was enhanced by catalase (Fig. 6, *E* and *F*) in small arteries.

Western blotting of eNOS protein expression in myocardium. In the control group, expression of eNOS protein in the ischemic LAD area was significantly decreased compared with the nonischemic LCX area (Fig. 7). In the catalase group, this decrease in the eNOS protein expression was inhibited by catalase (Fig. 7).

Endothelium-independent coronary vasodilatation. Coronary vasodilator responses to SNP were comparable under all conditions in both sized arteries (Fig. 8). Those coronary vasodilator responses were resistant to the blockade of NO synthesis with L-NMMA (Fig. 8).

Effect of H_2O_2 on I/R-induced myocardial infarct size. I/R injury caused myocardial infarction, the size of which was ~40% of the LV risk area (Fig. 9*A*). Intracoronary L-NMMA, catalase, or 8-SPT alone did not further increase the I/R-induced infarct size (Fig. 9*A*). By contrast, intracoronary L-NMMA plus catalase or TEA markedly increased the infarct size, and L-NMMA plus catalase with 8-SPT further increased

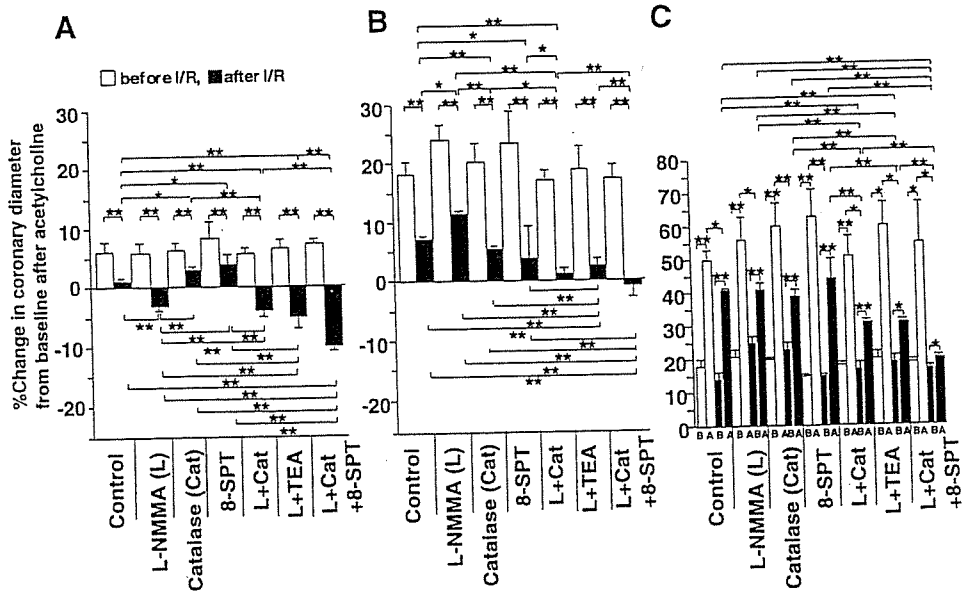

Fig. 3. Endothelium-dependent coronary vasodilatation to ACh before and after coronary I/R injury in dogs in vivo. *A*: small artery (≥100 μm). *B*: arteriole (<100 μm). *C*: coronary blood flow (CBF). No. of small arteries or arterioles per animals (*n/n*) used was 7/5 for control, 8/5 for L-NMMA, 10/5 for catalase, 6/5 for 8-SPT, 8/5 for L-NMMA plus catalase, 5/5 for L-NMMA plus TEA, and 5/5 for L-NMMA plus catalase plus 8-SPT in small arteries; and 12/5 for control, 16/5 for L-NMMA, 12/5 for catalase, 5/5 for 8-SPT, 10/5 for L-NMMA plus catalase, 8/5 for L-NMMA plus TEA, and 7/5 for L-NMMA plus catalase plus 8-SPT in arterioles. No. of animals during the measuring CBF used was 5 for each group. B, before ACh; A, after ACh. $*P < 0.05$, $**P < 0.01$.

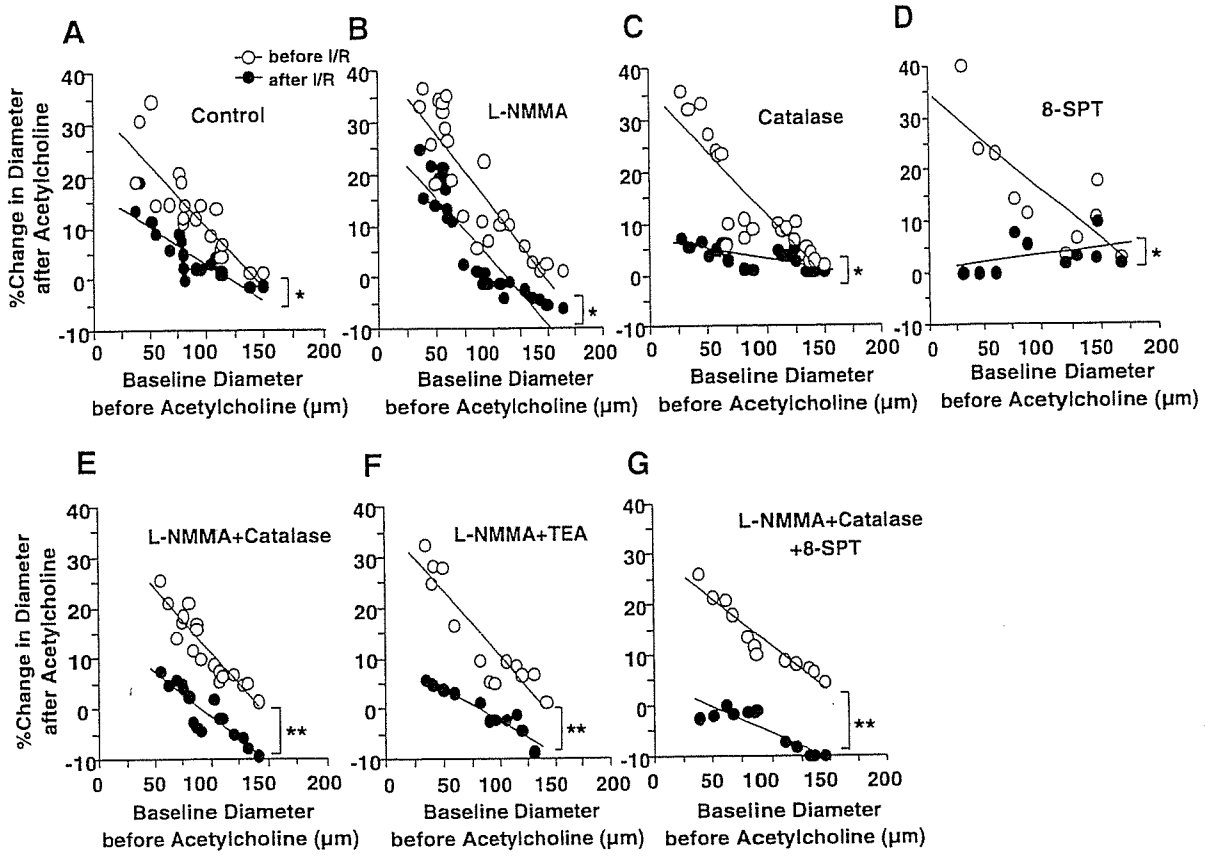

Fig. 4. Percent change in diameter after ACh before and after coronary I/R injury in dogs in vivo. No. of small arteries and arterioles per animals used was 7/5 for control (*A*), 8/5 for L-NMMA (*B*), 10/5 for catalase (*C*), 6/5 for 8-SPT (*D*), 8/5 for L-NMMA plus catalase (*E*), 5/5 for L-NMMA plus TEA (*F*), and 5/5 for L-NMMA plus catalase plus 8-SPT in small arteries (*G*); and 12/5 for control (*A*), 16/5 for L-NMMA (*B*), 12/5 for catalase (*C*), 5/5 for 8-SPT (*D*), 10/5 for L-NMMA plus catalase (*E*), 8/5 for L-NMMA plus TEA (*F*), and 7/5 for L-NMMA plus catalase plus 8-SPT in arterioles (*G*). $^*P < 0.05$, $^{**}P < 0.01$.

the infarct size (Fig. 9*A*). In the control group, there was an inverse relation between the infarct size and transmural collateral blood flow measured by microsphere technique ($r = 0.90$, $P < 0.01$). There was no significant difference in the relationship among the control, L-NMMA, and catalase treatment (Fig. 9*B*). L-NMMA plus catalase or TEA significantly shifted the regression line upward compared with the control group (both $P < 0.01$), and L-NMMA plus catalase with 8-SPT further shifted the regression line upward compared with L-NMMA plus catalase or TEA (Fig. 9*B*, both $P < 0.01$).

DISCUSSION

The major finding of the present study is that endogenous H_2O_2, in cooperation with NO, plays an important cardioprotective role during coronary I/R injury as a compensatory mechanism for NO in vivo. To the best of our knowledge, this is the first report that demonstrates the important protective role of endogenous H_2O_2, in cooperation with NO, against coronary I/R injury in vivo.

Validations of experimental model and methodology. On the basis of the previous reports (22, 31), we chose the adequate dose of ACh, SNP, L-NMMA, catalase, TEA, and 8-SPT to examine the effects of endothelium-dependent and -independent coronary vasodilator responses and inhibition of NO synthesis, H_2O_2, K_{Ca} channels, and adenosine receptor, respectively. In addition, on the basis of previous studies and our own (31, 35), we choose the doses of ACh and SNP that cause maximal coronary vasodilatation in dogs in vivo. TEA at low doses is fairly specific for K_{Ca} channel, but at higher doses it may block a number of other K channels. Because several K_{Ca} channels are involved in H_2O_2-mediated responses (26), we selected the nonselective K_{Ca} inhibitor TEA to inhibit all K_{Ca} channels (15). We have previously confirmed the validity of the methods that we used in the present study (32). After 60–90 min of ischemia, ultrastructural damage of coronary endothelium was observed particularly in the subendocardium in the present study, a finding consistent with the previous study (8).

H_2O_2 during coronary I/R in vivo. It was previously reported that relaxations of isolated large canine coronary arteries to exogenous H_2O_2 were partially endothelium dependent (23). Recently, Matoba et al. (16, 17) identified that endothelium-derived H_2O_2 is an EDHF in mouse and human mesenteric microvessels. Subsequently, we (35) and others (19) have confirmed that endogenous H_2O_2 exerts important vasodilator effects in canine coronary microcirculation in vivo and in isolated human coronary microvessels, respectively. It is conceivable that H_2O_2 is produced from superoxide anions derived from several sources in endothelial cells, including eNOS, cyclooxygenase, lipoxygenase, cytochrome *P*-450 enzymes, and NAD(P)H oxidases (16). In the present study, L-NMMA or catalase alone did not com-

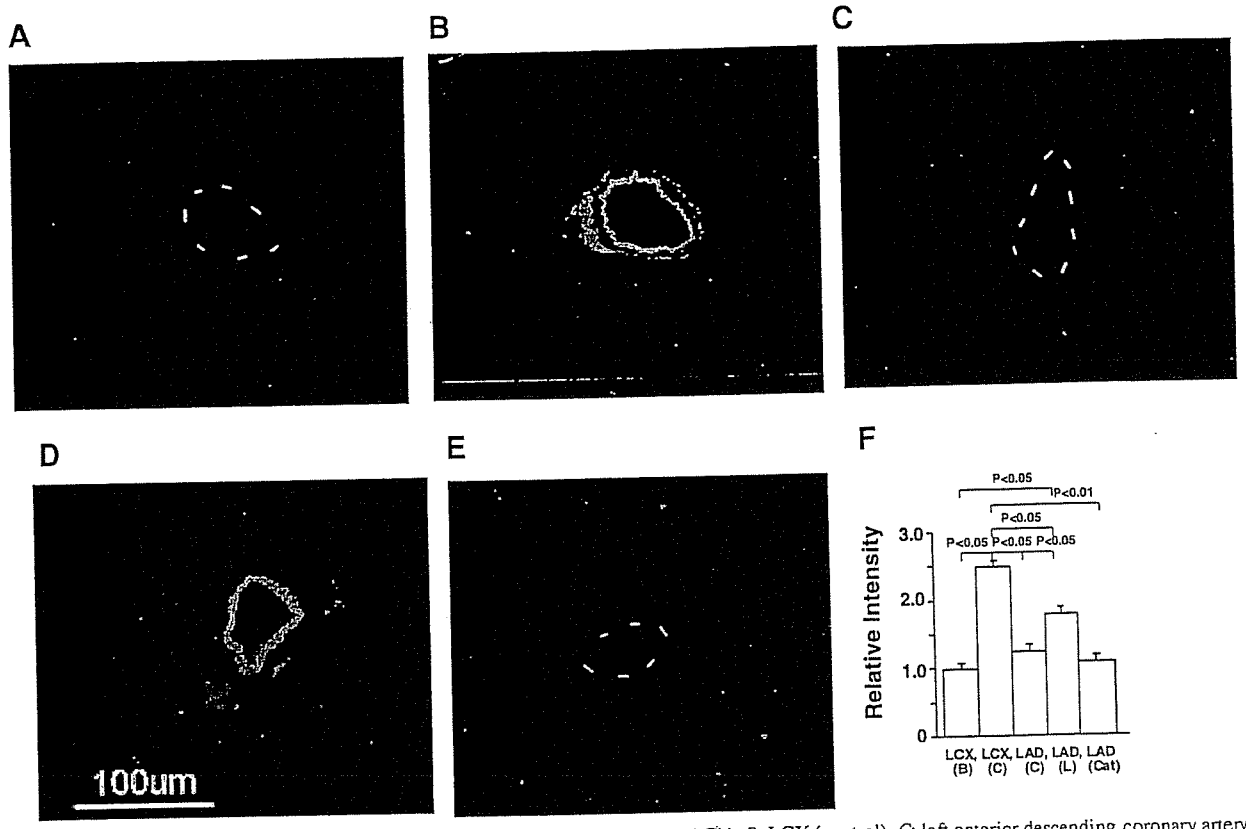

Fig. 5. Detection of H_2O_2 production. *A*: left circumflex artery (LCX; baseline without ACh). *B*: LCX (control). *C*: left anterior descending coronary artery (LAD; control). *D*: LAD (L-NMMA). *E*: LAD (catalase). *F*: fluorescent intensity (B, baseline without ACh; C, control, L, L-NMMA; Cat, catalase). No. of arterioles per animals used was 5/5 for each group. Dashed line, outline of vessels. Bar, 100 μm.

pletely abolish the ACh-induced vasodilatation in both sized arteries, whereas L-NMMA plus catalase markedly attenuated the residual vasodilatation in vivo as did TEA, indicating that H_2O_2 exerts important vasodilator effects during I/R injury in canine coronary microcirculation in vivo (Figs. 3 and 4). Furthermore, in the present study, endogenous H_2O_2-mediated coronary vasodilatation was noted to a greater extent in arterioles than in small arteries (Figs. 3 and 4), confirming the predominant role of H_2O_2 in microvessels and that of NO in relatively large arteries in vivo (25).

Compensatory vasodilator mechanism among H_2O_2, NO, and adenosine. It is well known that coronary vascular tone is regulated by the interactions among several endogenous vasodilators, including NO, H_2O_2, and adenosine (33). These vasodilators play an important role in compensatory vasodilatation of coronary microvessels during myocardial ischemia (35). In the present study (Figs. 3 and 4), endothelium-dependent arteriolar vasodilatation to ACh during coronary I/R was significantly increased by L-NMMA while small arterial vasodilatation to ACh was increased by catalase and 8-SPT, and the residual arteriolar dilation was further inhibited by both of them (L-NMMA plus catalase or TEA). Furthermore, fluorescent microscopy with DCF and DAR, respectively, showed that H_2O_2 and NO production after I/R were enhanced in small coronary arteries and arterioles by L-NMMA [fluorescent intensity (FI) 1.8] and catalase (FI 1.9) compared with those in the LAD of control group (Figs. 5 and 6, FI: DAR 1.2 and DCF 1.1). The residual small arteriolar dilatation after combined administration of L-NMMA + catalase was completely blocked by 8-SPT, an adenosine receptor blocker, indicating that adenosine also compensated for the loss of action of NO and H_2O_2. Taken together, these results indicate the compensatory vasodilator effects among NO, H_2O_2, and adenosine to maintain coronary blood flow during coronary I/R injury in vivo. H_2O_2 and NO were mutually compensatory in both small arteries and arterioles, and in the presence of their inhibitors (catalase and L-NMMA), adenosine also caused arteriolar vasodilatation, as we reported previously (35). This finding is consistent with our finding that NO, H_2O_2, and adenosine play an important compensatory role in coronary autoregulation in canine coronary microcirculation in vivo (35). It was reported that TEA inhibited adenosine-induced vasodilatation of canine subepicardial coronary arteries in vitro (3). Furthermore, H_2O_2 stimulates protein kinase C, phospholipase A_2, and arachidonic acid release and increases intracellular cAMP levels (10). These findings suggest that cAMP-mediated pathway is involved, at least in part, during coronary vasodilatation through K_{Ca} channels after I/R injury.

Role of H_2O_2 during coronary I/R. It is known that K_{Ca} channels substantially contribute to coronary vasodilatation in myocardial ischemia (22) and that H_2O_2 also activates K_{Ca} channels (11). However, it remains to be examined whether H_2O_2 contributes to coronary vasodilatation during I/R in vivo. The present results demonstrate that H_2O_2

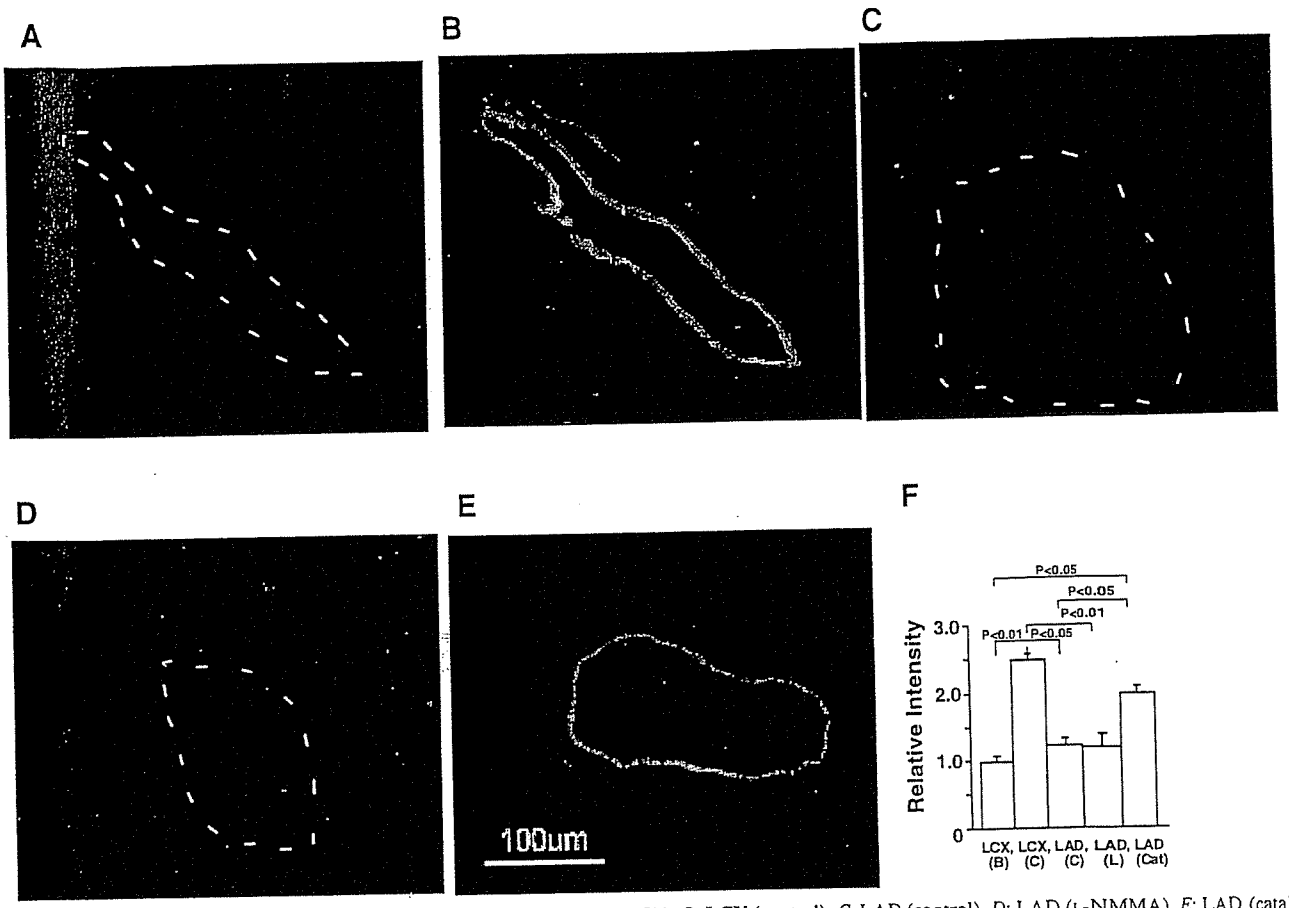

Fig. 6. Detection of nitric oxide (NO) production. *A*: LCX (baseline without ACh). *B*: LCX (control). *C*: LAD (control). *D*: LAD (L-NMMA). *E*: LAD (catalase). *F*: fluorescent intensity (B, baseline without ACh; C, control, L, L-NMMA; Cat, catalase). No. of small arteries per animals used was 5/5 for each group. Dashed line, outline of vessels.

substantially contributes to coronary vasodilatation during I/R in vivo as a compensatory mechanism for the loss of NO. Several mechanisms have been proposed for K_{Ca} channel opening during coronary I/R, including cellular acidosis

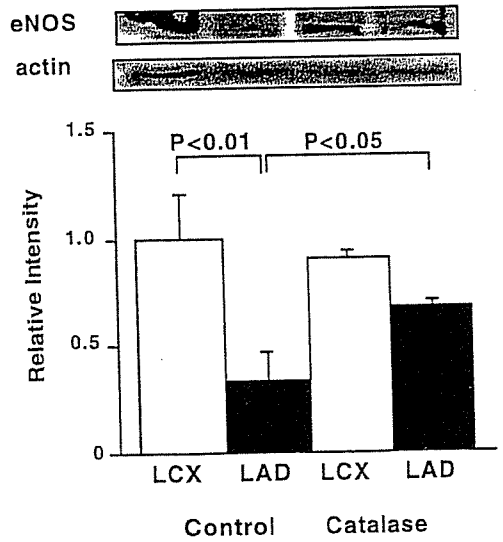

Fig. 7. Western blotting showing the effects of catalase on endothelial nitric oxide synthase (eNOS) protein expression in the myocardium of LAD and LCX. No. of animals used was 3 for each group.

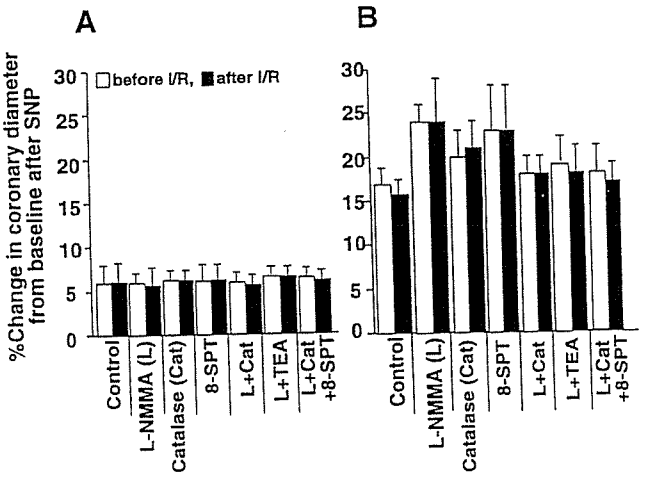

Fig. 8. Endothelium-independent coronary vasodilatation before and after coronary I/R injury in dogs in vivo. *A*: small artery (≥100 μm). *B*: arteriole (<100 μm). No. of small arteries and arterioles per animals used (*n*/*n*) was 7/5 for control, 8/5 for L-NMMA, 10/5 for catalase, 6/5 for 8-SPT, 8/5 for L-NMMA plus catalase, 5/5 for L-NMMA plus TEA, and 5/5 for L-NMMA plus catalase plus 8-SPT in small arteries; and 12/5 for control, 16/5 for L-NMMA, 12/5 for catalase, 5/5 for 8-SPT, 10/5 for L-NMMA plus catalase, 8/5 for L-NMMA plus TEA, and 7/5 for L-NMMA plus catalase plus 8-SPT in arterioles.

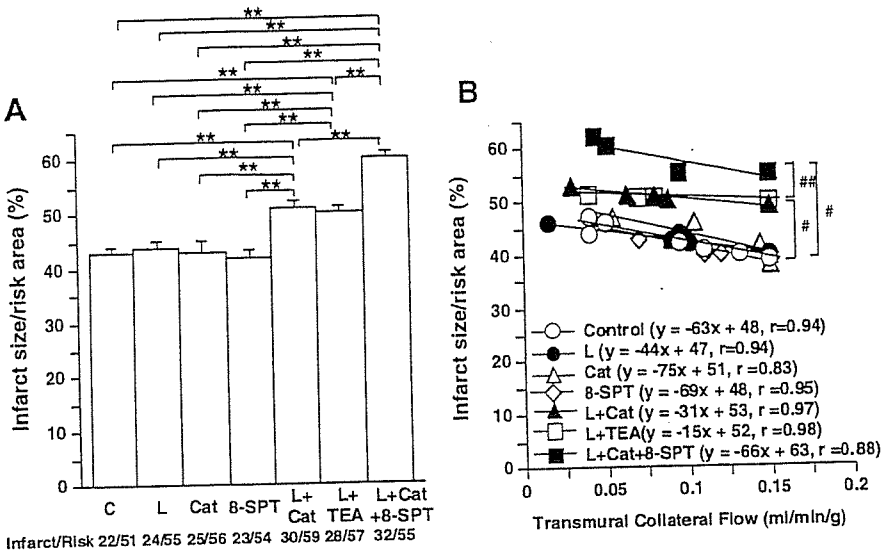

Fig. 9. Effects of H_2O_2, NO, and adenosine on I/R-induced MI in dogs in vivo. *A*: I/R-induced left ventricular infarct size in dogs in vivo. C, control. *B*: plot of infarct size expressed as a percentage of the risk area and regional collateral flow during I/R. $^{**}P < 0.01$, $\#P < 0.05$ vs. L-NMMA (L) or Cat or 8-SPT; $\#\#P < 0.01$ vs. L + TEA or L + Cat.

(27), increase in intracellular Ca^{2+} concentration after ischemia (28), and H_2O_2 production by inflammatory cells (5). Furthermore, an inhibitor of NO synthesis [N^G-nitro-L-arginine methyl ester (L-NAME)] or that of K_{Ca} channels (charybdotoxin) partly inhibits the protective effect on myocardial infarct size (22). Liu et al. (14) demonstrated that peroxynitrite inhibits K_{Ca} channel activity in human coronary arterioles during I/R. This mechanism might contribute to impaired H_2O_2-mediated dilation in I/R where NO synthase activity is increased in the presence of excess of O_2^-. In the present study, inhibition of H_2O_2 or NO alone did not significantly increase myocardial infarct size compared with control conditions (Fig. 9). These results suggest that H_2O_2 and NO exert cardioprotective effects against the development of myocardial infarction in a compensatory manner.

Recently, we have demonstrated that the expression of eNOS protein is decreased in the ischemic myocardium, which is improved by a selective Rho-kinase inhibitor, hydroxyfasudil, during coronary I/R injury in dogs in vivo (36). Furthermore, a physiological concentration (2 μmol/l) of H_2O_2 improved the recovery of both cardiac contractile function and energy metabolism after I/R in perfused rat heart (37). In the present study, the expression of eNOS protein was decreased in the ischemic myocardium, which was increased by catalase during I/R injury (Fig. 7). All these mechanisms may be involved in the beneficial effects of H_2O_2 on the I/R-induced myocardial injury. It also is conceivable that I/R reduces endothelial tetrahydrobiopterin levels in coronary vessels and impairs eNOS function (30).

Limitations of the study. Several limitations should be mentioned for the present study. First, we did not examine coronary vasodilatation in response to SOD/SOD mimetic (e.g., Tempol) or peroxynitrite inhibitor (e.g., ebselen) after I/R. However, because of the complex interactions among the oxygen species, we consider that both Tempol and ebselen also affect H_2O_2 metabolism by scavenging superoxide anions and peroxynitrite, respectively. Second, in addition to catalase, endogenous glutathione peroxidase (GSH) also plays an important role in removing H_2O_2, and NO also could be a substrate for endogenous catalase (1). However, in the present study, we used exogenous catalase to remove H_2O_2 to examine the role of the reactive oxygen species. Third, the exact source of vascular H_2O_2 production remains to be elucidated (e.g., the endothelium, smooth muscle, or cardiomyocytes). Fourth, while we were able to demonstrate the production of H_2O_2 using fluorescent microscopy with DCF, we were unable to quantitatively measure the H_2O_2 production because DCF detects H_2O_2, $ONOO^-$, and HOCl as well. Fifth, we were unable to find smaller arterioles because of the limited spatial resolution of our CCD intravital microscope. If we had an intravital camera with higher resolution, we would be able to observe coronary vasodilator responses of smaller arterioles.

Clinical implications and conclusions. During coronary I/R, microemboli of atherosclerosis debris and platelet plugs are released into the coronary microcirculation, particularly at revascularization with thrombolysis and/or percutaneous coronary intervention. Thus preexisting coronary endothelial dysfunction with various risk factors may be an important determinant for I/R injury in acute myocardial infarction. The synthesis and/or action of endothelium-derived NO are impaired under various pathological conditions, such as hypertension, hyperlipidemia, and diabetes mellitus (26, 34). In hypertension, K channel activities are increased in a compensatory manner with reduced NO activity (13). The present results suggest that NO and H_2O_2 compensate each other to cause coronary vasodilatation during I/R injury in vivo.

In conclusion, we were able to demonstrate that endogenous H_2O_2, in cooperation with NO, plays an important cardioprotective role in coronary I/R injury in vivo. The present findings may have important clinical implications because H_2O_2-mediated mechanisms substantially contribute to endothelium-dependent vasodilatation in coronary I/R in vivo.

GRANTS

This work was supported in part by grants from the Japanese Ministry of Education, Science, Sports, Culture, and Technology, Tokyo, Japan (Nos. 13307024, 13557068, 14657178, 15256003, 16209027, 16300164), and the Program for Promotion of Fundamental Studies in Health Sciences of the Organization for Pharmaceutical Safety and Research of Japan.

REFERENCES

1. Antunes F, Han D, and Cadenas E. Relative contributions of heart mitochondria glutathione peroxidase and catalase to H_2O_2 detoxification in in vivo conditions. *Free Radic Biol Med* 33: 1260–1267, 2002.
2. Bauersachs J, Hecker M, and Busse R. Display of the characteristics of endothelium-derived hyperpolarizing factor by a cytochrome *P*450-derived arachidonic acid metabolite in the coronary microcirculation. *Br J Pharmacol* 113: 1548–1553, 1994.
3. Cabell F, Weiss DS, and Price JM. Inhibition of adenosine-induced coronary vasodilation by block of large-conductance Ca^{2+} activated K^+ channels. *Am J Physiol Heart Circ Physiol* 267: H1455–H1460, 1994.
4. Campbell WB, Gebremedhin D, Pratt PF, and Harder DR. Identification of epoxyeicosatrienoic acids as an endothelium-derived hyperpolarizing factor. *Circ Res* 78: 415–423, 1996.
5. Chandrasekar B, Colston JT, de la Rosa SD, Rao PP, and Freeman GL. TNF-α and H_2O_2 induce IL-18 and IL-18R β expression in cardiomyocytes via NF-κB activation. *Biochem Biophys Res Commun* 303: 1152–1158, 2003.
6. Chen G, Suzuki H, and Weston AH. Acetylcholine releases endothelium-derived hyperpolarizing factor and EDRF from blood vessels. *Br J Pharmacol* 95: 1165–1174, 1988.
7. Edwards G, Dora KA, Gardener MJ, Garland CJ, and Weston AH. K^+ is an endothelium-derived hyperpolarizing factor in rat arteries. *Nature* 396: 269–272, 1998.
8. Ehring T, Krajcar M, Baumgart D, Kompa S, Hummelgen M, and Heusch G. Cholinergic and α-adrenergic coronary constriction with increasing ischemia-reperfusion injury. *Am J Physiol Heart Circ Physiol* 268: H886–H894, 1995.
9. Feletou M and Vanhoutte PM. Endothelium-dependent hyperpolarization of canine smooth muscle. *Br J Pharmacol* 93: 515–524, 1988.
10. Gao Y and Vanhoutte PM. Effects of hydrogen peroxide on the responsiveness of isolated canine bronchi: role of prostaglandin E_2 and I_2. *Am J Physiol Lung Cell Mol Physiol* 263: L402–L408, 1992.
11. Hayabuchi Y, Nakaya Y, Matsuoka S, and Kuroda Y. Hydrogen peroxide-induced vascular relaxation in porcine coronary arteries is mediated by Ca^{2+}-activated K^+ channels. *Heart Vessels.* 13: 9–17, 1998.
12. Huang A, Sun D, Carroll MA, Jiang H, Smith CJ, Connetta JA, Falck JR, Shesely EG, Koller A, and Kaley G. EDHF mediates flow-induced dilation in skeletal muscle arterioles of female eNOS-KO mice. *Am J Physiol Heart Circ Physiol* 280: H2462–H2469, 2001.
13. Liu Y, Hudetz AG, Knaus HG, and Rusch NJ. Increased expression of Ca^{2+}-sensitive K^+ channels in the cerebral microcirculation of genetically hypertensive rats: evidence for their protection against cerebral vasospasm. *Circ Res* 82: 729–737, 1998.
14. Liu Y, Terata K, Chai Q, Li H, Kleinman LH, and Gutterman DD. Peroxynitrite inhibits Ca^{2+}-activated K^+ channel activity in smooth muscle of human coronary arterioles. *Circ Res* 91: 1070–1076, 2002.
15. Masumoto A, Hirooka Y, Shimokawa H, Hironaga K, Setoguchi S, and Takeshita A. Possible involvement of Rho-kinase in the pathogenesis of hypertension in humans. *Hypertension* 38: 1307–1310, 2001.
16. Matoba T, Shimokawa H, Nakashima M, Hirakawa Y, Mukai Y, Hirano K, Kanaide H, and Takeshita A. Hydrogen peroxide is an endothelium-derived hyperpolarizing factor in mice. *J Clin Invest* 106: 1521–1530, 2000.
17. Matoba T, Shimokawa H, Kubota H, Morikawa K, Fujiki T, Kunihiro I, Mukai Y, Hirakawa Y, and Takeshita A. Hydrogen peroxide is an endothelium-derived hyperpolarizing factor in human mesenteric arteries. *Biochem Biophys Res Commun* 290: 909–913, 2002.
18. Mehta JL, Nichols WW, Donnelly WH, Lawson DL, and Saldeen TG. Impaired canine coronary vasodilator response to acetylcholine and bradykinin after occlusion-reperfusion. *Circ Res* 64: 43–54, 1989.
19. Miura H, Bosnjak JJ, Ning G, Saito T, Miura M, and Gutterman DD. Role for hydrogen peroxide in flow-induced dilation of human coronary arterioles. *Circ Res* 92: e31–e40, 2003.
20. Mori H, Haruyama Y, Shinozaki H, Okino H, Iida A, Takanashi R, Sakuma I, Husseini WK, Payne BD, and Hoffman JI. New nonradioactive microspheres and more sensitive X-ray fluorescence to measure regional blood flow. *Am J Physiol Heart Circ Physiol* 263: H1946–H1957, 1992.
21. Morikawa K, Shimokawa H, Matoba T, Kubota H, Akaike T, Talukder MA, Hatanaka M, Fujiki T, Maeda H, Takahashi S, and Takeshita A. Pivotal role of Cu,Zn-superoxide dismutase in endothelium-dependent hyperpolarization. *J Clin Invest* 112: 1871–1879, 2003.
22. Ogita H, Node K, Asanuma H, Sanada S, Liao Y, Takashima S, Asakura M, Mori H, Shinozaki Y, Hori M, and Kitakaze M. Amelioration of ischemia- and reperfusion-induced myocardial injury by the selective estrogen receptor modulator, raloxifene, in the canine heart. *J Am Coll Cardiol* 40: 998–1005, 2002.
23. Rubanyi GM and Vanhoutte PM. Oxygen-derived radicals, endothelium, and responsiveness of vascular smooth muscle. *Am J Physiol Heart Circ Physiol* 250: H815–H821, 1986.
24. Satoh M, Fujimoto S, Haruna Y, Arakawa S, Horike H, Komai N, Sasaki T, Tsujioka K, Makino H, and Kashihara N. NAD(P)H oxidase and uncoupled nitric oxide synthase are major sources of glomerular superoxide in rats with experimental diabetic nephropathy. *Am J Physiol Renal Physiol* 288: F1144–F1152, 2005.
25. Shimokawa H, Yasutake H, Fujii K, Owada MK, Nakaike R, Fukumoto Y, Takayanagi T, Nagao T, Egashira K, Fujishima M, and Takeshita A. The importance of the hyperpolarizing mechanism increases as the vessel size decreases in endothelium-dependent relaxations in rat mesenteric circulations. *J Cardiovasc Pharmacol* 28: 703–711, 1996.
26. Shimokawa H. Primary endothelial dysfunction: atherosclerosis. *J Mol Cell Cardiol* 31: 23–37, 1999.
27. Siegel G, Emden J, Wenzel K, Mironneau J, and Stock G. Potassium channel activation in vascular smooth muscle. *Adv Exp Med Biol* 311: 53–72, 1992.
28. Steenbergen C, Murphy E, Levy L, and London RE. Elevation in cytosolic free calcium concentration early in myocardial ischemia in perfused rat heart. *Circ Res* 60: 700–707, 1987.
29. Taylor HJ, Chaytor AT, Evance WH, and Griffith TM. Inhibition of the gap junctional component of endothelium-dependent relaxations in rabbit iliac artery by 18-alpha glycyrrhetinic acid. *Br J Pharmacol* 125: 1–3, 1998.
30. Tiefenbacher CP, Chilian WM, Mitchell M, and Defily DV. Restoration of endothelium-dependent vasodilation after reperfusion injury by tetrahydrobiopterin. *Circulation* 94: 1423–1429, 1996.
31. Traverse JH, Chen Y, Crampton M, Voss S, and Bache RJ. Increased extravascular forces limit endothelium-dependent and -independent coronary vasodilation in congestive heart failure. *Cardiovasc Res* 52: 454–461, 2001.
32. Yada T, Hiramatsu O, Kimura A, Goto M, Ogasawara Y, Tsujioka K, Yamamori S, Ohno K, Hosaka H, and Kajiya F. In vivo observation of subendocardial microvessels of the beating porcine heart using a needle-probe videomicroscope with a CCD camera. *Circ Res* 72: 939–946, 1993.
33. Yada T, Hiramatsu O, Kimura A, Tachibana H, Chiba Y, Lu S, Goto M, Ogasawara Y, Tsujioka K, and Kajiya F. Direct in vivo observation of subendocardial arteriolar responses during reactive hyperemia. *Circ Res* 77: 622–631, 1995.
34. Yada T, Goto M, Hiramatsu O, Tachibana H, Toyota E, Nakamoto H, Ogasawara Y, Matsuda H, Arakawa K, Hayashi K, Suzuki H, and Kajiya F. In vivo visualization of subendocardial arteriolar response in renovascular hypertensive hearts. *Am J Physiol Heart Circ Physiol* 284: H1785–H1792, 2003.
35. Yada T, Shimokawa H, Hiramatsu O, Kajita T, Shigeto F, Goto M, Ogasawara Y, and Kajiya F. Hydrogen peroxide, an endogenous endothelium-derived hyperpolarizing factor, plays an important role in coronary autoregulation in vivo. *Circulation* 107: 1040–1045, 2003.
36. Yada T, Shimokawa H, Hiramatsu O, Kajita T, Shigeto F, Tanaka E, Shinozaki Y, Mori H, Kiyooka T, Katsura M, Ohkuma S, Goto M, Ogasawara Y, and Kajiya F. Beneficial effect of hydroxyfasudil, a specific Rho-kinase inhibitor, on ischemia-reperfusion injury in canine coronary microcirculation in vivo. *J Am Coll Cardiol* 45: 599–607, 2005.
37. Yaguchi Y, Satoh H, Wakahara N, Katoh H, Uehara A, Terada H, Fujise Y, and Hayashi H. Protective effects of hydrogen peroxide against ischemia/reperfusion injury in perfused rat hearts. *Circ J* 67: 253–258, 2003.

植物性ポリフェノールによる核内受容体 PPAR の活性化

井上裕康[1]、中田理恵子[1]、竹内悠[1]、塚本朋子[1]、堀田真理子[1]、名村尚武[2]
(奈良女子大・生活環境・食物栄養[1]) (Moorehouse 大学医学部神経生物[2])
inoue@cc.nara-wu.ac.jp

我々は誘導型シクロオキシゲナーゼ(COX-2)に関する研究を進め、核内受容体 PPARγが COX-2 の細胞特異的発現調節に関与することを報告した(1)。一方、赤ワインに含まれるフィトアレキシンであるレスベラトロールが、細胞特異的に COX-2 の発現を抑制することを見出し、核内受容体を介して COX-2 の発現を調節していると予想した。検討の結果、1)レスベラトロールが PPARα及び PPARγを選択的に活性化すること、2) 脳虚血実験モデルマウスにおいて、レスベラトロール(20 mg/kg)の 3 日間経口投与が脳保護効果を持つこと、3)PPARα選択的活性化剤 Fenofibrate や Wy-14643 の経口投与が同様に脳保護効果を持つこと、4)レスベラトロール経口投与による脳保護効果は PPARα遺伝子欠損マウスでは消失することを見出した。したがって、レスベラトロールによる PPARαの活性化は、中等度のワイン消費が心血管病、脳卒中、痴呆の危険度と負の相関を示す、いわゆる「フレンチパラドックス」において、PPAR を介する新しい作用機構が関与すると考え研究を進めている(2)。さらに、レスベラトロール以外の植物性ポリフェノールについて検討した結果、PPAR 活性化能を持つものをいくつか見出した。レスベラトロールを含めたポリフェノール類の作用は、一般に抗酸化活性に起因していると考えられているが、PPAR 活性化能と抗酸化活性能との間に相関は認められなかった。

【目的】 「フレンチパラドックス」という言葉は、中等度の赤ワイン消費が心血管病、脳卒中、痴呆の危険度と負の相関を示すことに由来している。赤ワインには、レスベラトロールと呼ばれるフィトアレキシン（抗菌性物質）が含まれており、このレスベラトロールの抗酸化活性が、「フレンチパラドックス」に関与していると考えられてきた。我々はプロスタグランジン産生の律速酵素である誘導型シクロオキシゲナーゼ(COX-2)の発現制御について、種々の疾患における役割を視野に入れて研究を続けている(1),(3)-(8)。その共同研究の中で、レスベラトロールが COX-2 の酵素活性や発現誘導を阻害することを報告した(6)。そこで種々の細胞でレスベラトロールの効果をさらに検討した結果、COX-2 の発現は細胞の種類によって異なっていることを見出した（未発表）。一方、一連の実験から、マクロファージにおいて COX-2 発現はマクロファージで合成された PGD_2 代謝産物 15-deoxy-$\Delta^{12,14}$ PGJ_2 (15d-PGJ_2)が PPARγのリガンドとして作用することによって

負のフィードバック制御を受けることを報告した[1]。この二つの研究結果を考慮すると、15d-PGJ2 と同様に、レスベラトロールがある種の核内受容体リガンドとして作用しているのではないかいう着想を得たので、その可能性を検討した。

【方法及び結果】

レスベラトロールはPPARα及びPPARγの選択的デュアルアゴニスト

PPARα及び PPARγの発現ベクターとともに PPRE(ペルオキシソーム増殖剤応答配列)を持つレポーターベクターを種々の細胞に導入した。導入後、24 時間 10 μM レスベラトロールで処理すると、いずれの細胞においても PPARα及び PPARγの活性化が検出された(Fig. 1)。したがって、レスベラトロールによるこの活性化は種を越えて認められる。なお、その他の核内受容体のリガンドになる可能性についても検討を行ったが、レスベラトロールと同様な活性を持つものは見出されなかった。レスベラトロールはエストロゲン受容体のアゴニストとして働くという報告が以前になされているが、我々のレポーターアッセイ、および、BEACON2000 を用いた結合試験においても、弱い相互作用をするものの、報告されているようなエストロゲンアゴニスト活性は認められなかった。

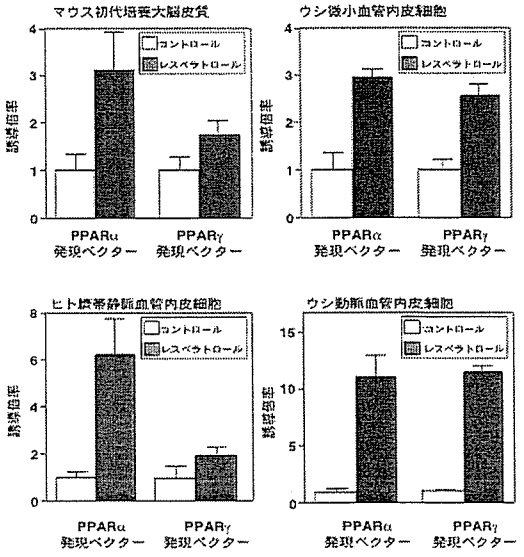

Fig. 1　ニューロン及び血管内皮細胞における
レスベラトロールによるPPAR応答エレメント活性化

レスベラトロールの PPARαを介する脳保護効果

以下に示す脳卒中実験モデルを用いて、脳保護効果を検討した(Fig. 2)。レスベラトロール (a)(d), Fenofibrate (b), Wy-14643 (c)を３日間経口投与後、中大脳動脈を血管内挿入したナイロン糸で閉塞し、脳血流量を遮断した。24 時間後、脳を摘出して切片(2mm)にした後、組織染色(2,3,5-triphenyltetrazolium)を行い、脳梗塞の体積を求めて評価した。レスベラト

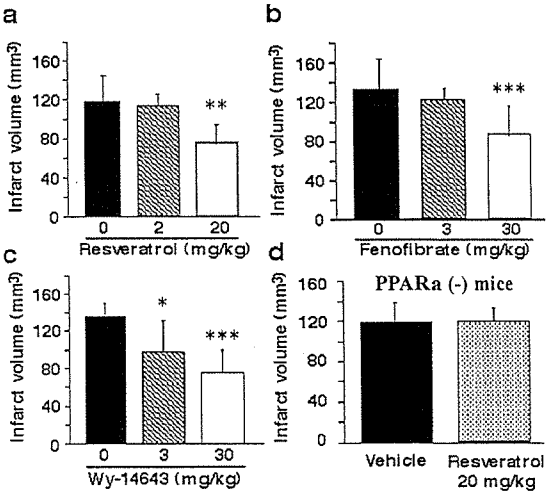

Fig. 2　レスベラトロールのPPARαを介する
脳保護効果

ロール経口投与は、PPARαアゴニストである Fenofibrate や Wy-14643 の経口投与と同様に脳保護効果が認められた(Fig. 2a, b, c)。しかし、レスベラトロールによる脳保護効果はPPARαノックアウトマウスでは認められなかった(Fig. 2d)。したがって、レスベラトロールによる脳保護効果は PPARαの活性化を介していると考えられた。なお、レスベラトロールによる脳保護効果は１日の経口投与では認められず、少なくとも３日以上の経口投与が必要であった。この知見は「フレンチパラドックス」における赤ワインの継続的飲酒に関係している可能性がある。また、赤ワイン中に含まれるレスベラトロールの含量は、葡萄の品種や栽培条件によって２桁以上異なり、紫外線照射や細菌の感染などによっても上昇する。さらに、他の食物中に含まれる PPARα活性化物質を考慮すれば、今回脳保護効果が認められたレスベラトロールの投与量は、赤ワイン飲酒とそれほどかけ離れていないと考えられる。この点も含めて、その分子作用機構の解明が必要である。

レスベラトロール経口投与による遺伝子発現の変動

レスベラトロール(20mg/kg)を一週間投与後、肝臓における遺伝子発現を DNA チップにより現在解析を行っている。RT-PCR 法による検討の結果(Fig. 3)、Cyp4a14 及び ApoA5 の発現が誘導されることを見出した。これらの遺伝子はいずれも PPRE を持つことから、レスベラトロール経口投与により PPARα活性化によって、下流で働く遺伝子群の候補であると考えられた。実際、これらの遺伝子については、PPARαアゴニスト投与により、誘導されることが既に報告されている。興味深い事に、Cyp4a14は脂肪酸ω水酸化酵素であり、この酵素が誘導されることで、新たな PPARαアゴニストが生成される可能性もある。

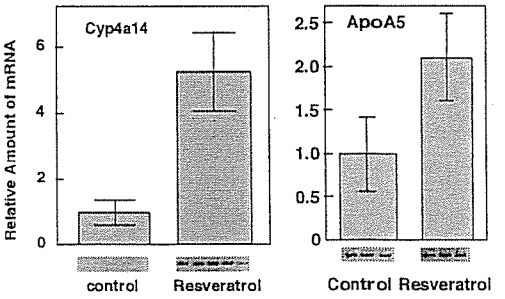

Fig. 3 レスベラトロール投与による遺伝子発現の増加

その他の植物性ポリフェノールによる PPAR 活性化の検討

レスベラトロール以外のポリフェノール類について、Fig. 1 と同様なアッセイ系によって PPAR 活性化能を検討した。その結果、パセリ、紫蘇、カモミールに含まれるアピゲニンがレスベラトロールに匹敵するほどの PPAR 活性化を示した(Fig. 4)。興味深いことに、アピゲニンによる活性化は PPARαに対してより、PPARγに対して相

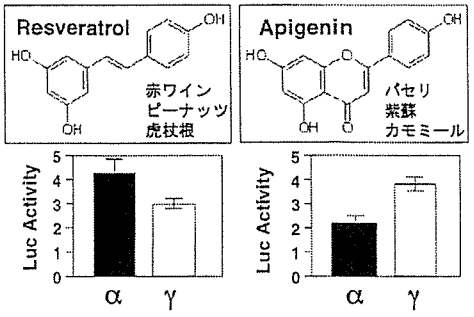

Fig. 4 アピゲニンのPPAR活性化能

対的に強い活性を示し、レスベラトロールとは異なっていた。レスベラトロールとアピゲニンの化学構造に着目すると、水酸基３個の位置が一致していることがわかり、これが PPAR との結合に重要であると考えられ、現在解析を進めている。一方、植物性ポリフェノールの抗酸化活性について、(1,1-diphenyl-2-picrylhydrazyl radical) DPPH の消去活性により評価した。その結果、PPAR 活性化能とラジカル消去活性は必ずしも一致しないことがわかった。したがって、PPAR 活性化能と抗酸化活性能との間に相関はないと考えられた。

【考察】レスベラトロールに関しては、最近、カロリー制限模倣物質として、寿命延長効果があることが報告されている。一方で、PPARαの新しい内因性リガンド候補として見出されたオレイルエタノールアミドが PPARα活性化によって食欲をコントロールすることも報告されている。したがって、PPAR 活性化—カロリー制限—長寿効果がつながっていく可能性がでてきた。さらに、アピゲニンに関しては、既に COX-2 の発現を抑制することが報告されている。共同研究の結果、γ-Mangostin や Chrysin などが COX-2 の発現を抑制することもわかってきた。興味深いことに、植物生理学の分野において、COX の活性阻害作用を持つサリチル酸はフィトアレキシンの産生を引き起こす物質として知られている。したがって、レスベラトロールにとどまらず、食品中に含まれるその他のポリフェノール類と核内受容体や COX 経路との相互作用は、寿命延長、生活習慣病予防の視点から、今後さらに研究が進んでいくと考えられる。

文献

(1) Inoue, H., et al.: *J. Biol. Chem.* **275,** 28028-28032 (2000)
(2) Inoue, H., et al.: *Neurosci. Lett.* **352,** 203- 206 (2003)
(3) Inoue, H., et al.: *FEBS Lett.*, **350,** 51-54 (1994)
(4) Inoue, H., et al.: *J. Biol. Chem.* **270,** 24965-24971 (1995)
(5) Inoue, H., Tanabe, T.: *Biochem. Biophys. Res. Commun.* **244,** 143-148 (1998)
(6) Subbaramaiah, K., et al.: *J. Biol. Chem.* **273,** 21875-21882 (1998)
(7) Inoue, H., et al.: *Biochem. Biophys. Res. Commun.* **254,** 292-298 (1999)
(8) Inoue, H., et al.: *Artherioscler. Thromb. Vasc. Biol.* **22,** 1415-1420 (2002)

【解説】

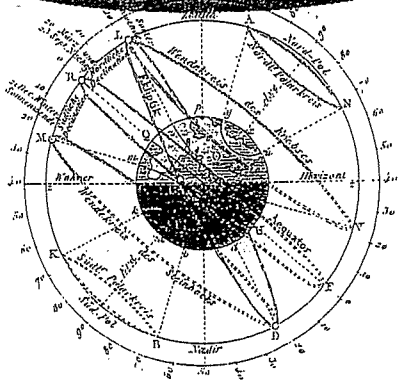

トランスポータ研究のいま
Na^+/H^+ 交換輸送体を中心に

久光　隆，若林繁夫

膜を隔てた物質輸送を行なうトランスポータはあらゆる生物の生存に根源的である．物質がタンパク質の間をどのように透過するのか？　物質輸送がどのように制御されるのか？これらのミステリーが結晶構造解析などによって今，解かれようとしている．最近の魅力的なトランスポータ研究を紹介するとともに，著者らが主として研究対象としている生体pH制御に重要な役割を担う Na^+/H^+ 交換輸送体の構造と生理機能について最近の知見を解説する．

生命は，原始の海で膜によって閉じられた構造をつくることによって始まったとされる．これは，閉じられた空間によって物質が濃縮され，希薄溶液中ではなしえなかった低分子有機化合物から高分子化合物への化学反応が可能となったためであると考えられている．生命の誕生にはこのような外(海)とは区別された環境をつくり出すことが必須の条件であったと考えられる．進化の過程を経て今のような姿になった細胞には膜によって独立した空間がつくられ，さらに細胞内にはさまざまな細胞内小器官がまた同様の膜構造を形成している．細胞内においても細胞質側と細胞内小器官内とでは環境が異なっている．これら生体膜は主にリン脂質とタンパク質で構成されている．リン脂質は両親媒性の物質で，低分子の脂溶性化合物以外の水溶性有機化合物やイオンを透過させず，バリアーとして機能している．しかし細胞は，その生命活動を維持するために，それら物質の出入りを必要に応じて制御し，恒常性を保たなくてはならない．その物質の透過路を担うのが生体膜に存在するトランスポータ，チャネル，ポンプに分類される一群の膜タンパク質である（図1）．本稿では，トランスポータに関する最近のブレイクスルー的な研究を概説したのち，一つの重要なトランスポータファミリーである Na^+/H^+ exchanger (NHE/SLC9) の構造・機能および生理的・病態的意義について，筆者らのこれまでの知見を中心に解説する．

Recent Topics on Membrane Transporter, Particularly on the Na^+/H^+ Exchanger Family
Takashi HISAMITSU, Shigeo WAKABAYASHI, 国立循環器病センター研究所循環分子生理部

トランスポータの作動機構

トランスポータはすべての細胞および細胞内小器官において，無機イオン，栄養物質，薬物などさまざまな物質を輸送する．輸送基質の選択性が厳格かそうでないかは，トランスポータの種類によって異なる．トランスポータは，必要なものは取り込み，不要なものは排出するという単純明快な役割を担うことによって細胞ひいて